Classification of human actin pathological variants using *C. elegans* CRISPR-generated models

Théo Hecquet[1,2, 3, 4], Nadine Arbogast[1,2, 3, 4], Delphine Suhner[1,2, 3, 4], Anaïs Goetz[1,2, 3, 4], Grégory Amann[1,2, 3, 4], Selin Yürekli[1,2, 3, 4], Fiona Marangoni[1,2, 3, 4], Johannes N. Greve[5], Nataliya Di Donato [6], Anne-Cécile Reymann[1,2, 3, 4]

1. Université de Strasbourg, *IGBMC UMR 7104- UMR-S 1258, F-67400 Illkirch, France*
2. CNRS*, UMR 7104, F-67400 Illkirch, France*
3. Inserm, *UMR-S 1258, F-67400 Illkirch, France*
4. *IGBMC, Institut de Génétique et de Biologie Moléculaire et Cellulaire, F-67400 Illkirch, France*
5. Institute for Biophysical Chemistry, Hannover Medical School, Fritz–Hartmann–Centre for Medical Research, 30625 Hannover, Germany
6. Department of Human Genetics, Hannover Medical School, 30625 Hannover, Germany

Abstract

Actin plays a crucial role in diverse physiological processes via the formation of dynamic networks that determine cellular shape and mechanical properties. *De novo* variants in cytoskeletal β- and γ-actin, encoded by human *ACTB* and *ACTG1* genes, lead to a wide range of rare diseases, termed Non-Muscle Actinopathies (NMA). Variants include missense, frameshift, truncating variants up to whole gene deletions and induce diverse symptoms. So far, the high clinical variability and genotype-phenotype correlations in NMA remain largely unresolved. To address this question, we used CRISPR to insert in the *C. elegans* homologue *act-2* gene nine *de novo* mutations identified in patients. Using these animal models, we performed a quantitative multiscale characterisation. We uncovered a variety of perturbations: actin network defects at the micro scale, cell scale abnormalities, morphogenesis failure, as well as weaker behavioural phenotypes. Importantly, the range of developmental defects observed correlates with the severity of patients' symptoms. Thus, we provide evidence that a *C. elegans*-based approach represents a new way to investigate the mechanisms underlying NMA physiopathology or ultimately screen for therapeutic strategies.

Keywords

C. elegans, cytoplasmic actin, Non-Muscle Actinopathy, Baraitser-Winter Cerebrofrontofacial Syndrome

I. Introduction

The ability to dynamically assemble the actin cytoskeleton in response to internal and external triggers is a hallmark of a healthy and functional cell. The combination of finely tuned actin architectures in coordination with specific cellular needs and constant reorganization while adapting to external cues, drive a multitude of cellular processes including motility, adhesion, internal organisation and trafficking, morphogenesis or mechanotransduction (Blanchoin et al. 2014; Murrell et al. 2015). Degenerated cytoskeletal integrity is directly involved in many disorders ranging from hearing loss to cancer or rare diseases (Parker, Baboolal, and Peckham 2020; Lai and Wong 2020). The human genome encodes six highly conserved actin isoforms, which are produced in a time- and tissue-specific manner and every actin isoform has been associated with human pathologies (Parker, Baboolal, and Peckham 2020). *De novo* missense variants, frameshift or truncating variants as well as gene deletions in the *ACTB* and *ACTG1* genes, which encode the ubiquitously expressed cytoplasmic β- and γ-actin, cause substantial cellular dysfunction and lead to a range of rare disorders, termed Non-Muscle Actinopathies (NMA) (Cuvertino et al. 2017; Latham et al. 2018; Polubothu et al. 2020; Rivière et al. 2012; Verloes et al. 2015; 1993). One particularity of these ultra-rare diseases is the broad spectrum of symptoms described in patients, that range from very mild to severe with detrimental effects on the life expectancy of the affected patients. So far, 287 patients and 157 unique mutations have been reported to cause NMA. The most frequently associated NMA disease, named Baraitser-Winter cerebrofrontofacial syndrome (BWCFF), is associated with characteristic facial malformations, intellectual disability, cortical malformations, epilepsy, hearing loss and a variety of congenital anomalies (Rivière et al. 2012; Verloes et al. 2015). Even within this subclass of NMA, a large range of symptom severity is observed.

To date, a definitive genotype-phenotype correlation within the NMA field has yet to emerge, and the functional mechanisms causing symptoms in patients remain largely elusive. The complexity may originate from both the multifaceted roles of actin and its numerous molecular partners (Actin Binding Proteins, ABP). Furthermore, the existence of compensatory mechanisms between isoforms constitute a challenge in the study of actin *in vivo* (Dugina et al. 2009; Vedula et al. 2017; Boiero Sanders et al. 2022; Michelot and Drubin 2011). Actin variants have been proposed to affect the cytoskeleton by four mechanisms: haploinsufficiency leading to insufficient availability of actin monomers, alteration of the actin filament assembly or disassembly kinetics, alteration of actin interactions with binding partners and assembly of toxic actin oligomers detrimental for proper cytoskeletal function (Greve et al. 2023). At the structural

level, *in silico* models correlated some NMA mutations with nucleotide-binding, monomer-monomer interaction and canonical G-actin-ABP interaction surfaces (Latham et al. 2018). In addition, the use of purified recombinant human actin proteins allowed to quantitatively assess defects in terms of folding, thermal stability, nucleotide-binding, G- to F-actin transition or interaction with ABPs for some variants (Greve et al. 2023; 2022), validating some of these hypotheses. *In vivo*, the effects of *ACTB* and *ACTG1* deletions have been studied in mouse embryonic fibroblasts and in the whole animal (Patrinostro et al. 2018; Bunnell and Ervasti 2010; Bunnell et al. 2011)**.** Notably, *ACTB* deletion leads to proliferation defects in mouse embryonic fibroblasts as well as mice embryonic lethality, while *ACTG1* null mutant mice are viable (Vanslembrouck, Ampe, and Van Hengel 2020). However, a comprehensive system capable of bridging these different scales and validating the suggested molecular to functional relationship is still missing.

To fill this gap, we chose to use the free-living nematode *Caenorhabditis elegans* (*C. elegans*) as a model to study NMA, as it allows an easy access to all biologically relevant scales: from general animal fitness to stereotypical organization and development, up to cell-scale events and single molecular dynamics *in vivo*. *C. elegans* has already been used as a valid model for numerous diseases, notably for the study of neurodegenerative and neuromuscular disorders (Markaki and Tavernarakis 2010), thus demonstrating its capabilities in assessing the molecular to functional link in human diseases. The ease of genetic manipulation and the ability to obtain a stable, isogenic strains within a matter of weeks streamlines the process of strain characterization and enables us to investigate the consequences of multiple NMA variants in a reasonable amount of time.

In this study, we assess the consequences of actin variants associated with BWCFF or other NMA in a model organism, and present a quantitative multiscale characterization of *C. elegans* mutants. As cytoplasmic actin is required pleiotropically, we performed a global survey of mutants using well-established methods to assay both nematode fitness and specific organ function. We propose a classification of selected NMA variants with respect to the observed phenotypes in *C. elegans* and compare this classification to the severity of the patient's symptoms. This initial study of actin variants showed a strong correlation in the degree of severities between *C. elegans* and human, validating the use of *C. elegans* as a valuable tool to study NMA. Importantly, this work paves the way towards the prediction of clinical severity in patients carrying unknown actin variants.

II. Results

C. elegans cytoplasmic actin genes

Similarly to humans, *C. elegans* relies on different cytoplasmic actin paralogs to sustain cellular cytoskeleton integrity in all cell types. Three ubiquitously expressed actin genes (*act-1, act-2* and *act-3*) are present in a cluster and are operating in a partially redundant manner, notably during early embryogenesis (Hayashi, Ono, and Ono 2019; Willis et al. 2006; S. Ono and Pruyne 2012). These three cytoplasmic *C. elegans* actins are also required for proper muscle function (S. Ono 2014). Indeed, some mutations in the *act-2* gene were described to exhibit uncoordinated adult movement or pharyngeal pumping defects (Krause et al. 1989; Landel et al. 1984; Avery 1993; Willis et al. 2006). A fourth actin coding gene named *act-4* is also expressed in different tissues, notably in neurons and in muscle cells. However, it is not as enriched and ubiquitously expressed in the early embryo as one would expect for an essential cytoplasmic actin- as *act-1, act-2, act-3* (Serobyan et al. 2020). *act-5,* in contrast, shows a strong tissue-specific expression in the gut and excretory cell (MacQueen et al. 2005). With respects to the three *C. elegans* cytoplasmic actin genes: while *act-1* and *act-3* share identical coding sequences, they differ from *act-2* by three non-synonymous and many silent variations as well as distinct intronic regions. This allows a slightly facilitated CRISPR/Cas9 genome editing for *act-2* than for the others (Paix et al. 2015). Furthermore, ACT-2 has the highest similarity to human actin, sharing 98% of amino acids with *ACTB* and 97% with *ACTG1* (Figure S1A). Therefore, we decided to insert a series of genetic modifications identified in the human *ACTB* and *ACTG1* genes into the *C. elegans act-2* locus.

Generation of *C. elegans* models recapitulating human non-muscle actinopathies

Most human non-muscle actinopathies (NMA) are associated with severe neurological impairment and cortical malformations, although some patients do show either milder symptoms or oppositely, a shortened life span. In order to span the range of severities observed in human, we chose to study an initial set of nine mutations which included mutations associated with BWCFF (*ACTB* p.L65V, *ACTB* p.G74S, *ACTB* p.G74V, *ACTB* or *ACTG1* p.T120I, *ACTB* p.R196C, *ACTB* p.R196H and *ACTG1* p.T203M) (Verloes et al. 2015; Chacon-Camacho et al. 2020; Vontell et al. 2019); as well as non-BWCFF NMA diseases (*ACTB* p.R147S and *ACTB* or *ACTG1* p.R183W) (Figure 1). Among them, p.R196 is a hot-spot identified in over 19 patients,

presenting clinical variability with a high degree of brain malformation (83%, Figure 1C;REF NDD (Verloes et al. 2015; Cianci et al. 2017). Non-BWCFF variant p.R147S is a hotspot postzygotic *ACTB* mutations leading to mosaic skin disorders known as Becker nevus syndrome (Cai et al. 2017), possibly this variant might be lethal as a homozygous (Happle 2017); while p.R183W is associated with dystonia deafness (Eggink et al. 2017; Conboy et al. 2017; Gearing et al. 2002; Procaccio et al. 2006; Zech et al. 2017; Skogseid et al. 2018; Freitas et al. 2019).

We mapped the mutated residues investigated in this study on a structural model of the *C. elegans* ACT-2 monomer (G-actin) and filament to assess possible localisation of the variants in different regions of the molecule identified with specific functions (Figure 1A). The variants are distributed across all four subdomains (SD) of the actin monomer. Two variants (p.G74V/S, p.R183W) are located within the nucleotide-binding cleft and, although not directly involved in nucleotide coordination or hydrolysis, contribute significantly to the release of inorganic phosphate (P_i) following ATP hydrolysis (Oosterheert et al. 2023). The p.R147S variant is part of the target-binding cleft of the actin monomer, located between SD1 and SD3, which is lined with predominantly hydrophobic residues and represents a main interaction interface for G-actin binding proteins (Bunnell and Ervasti 2010; Dominguez and Holmes 2011). Variant p.T120I is part of the so-called pathogenic helix of actin (K113-T126), which constitutes a hotspot for mutations in several human actin isoforms leading to BWCFF (cytoskeletal β- and γ-actin), non-syndromic hearing loss (cytoskeletal γ-actin), thoracic aortic aneurysm (smooth muscle α-actin) and nemaline myopathy (skeletal muscle α-actin) (as reviewed in (Rubenstein and Wen 2014). Variants p.R196C/H and p.T203M are both located in SD4 and are part of regions of the actin monomer that are heavily involved in the formation of monomer-monomer contacts within the actin filament due to formation of a salt bridge by the neighbouring residue E195. T203 is part of a threonine-rich loop that contributes to lateral and longitudinal contacts in the filament (Dominguez and Holmes 2011; Reynolds et al. 2022). The p.L65V variant is located in SD2 in close proximity to the DNase-loop that contributes to lateral and longitudinal interfaces and undergoes structural rearrangement upon nucleotide hydrolysis, directly affecting filament stability (Oosterheert et al. 2023; Reynolds et al. 2022).

Using these selected variants associated with various human symptoms, we generated strains harbouring each selected NMA mutation in the *act-2* gene using CRISPR/Cas9 gene editing (Figure 1B). We verified that no additional mutations were present in all four other actin genes and backcrossed the strains several times before analysis. Additionally, we generated

two new null alleles for *act-2* (*rey016* and *rey021*) (Figure 1B), resulting both in a premature STOP codon within exon 2 (see methods section for more details). For comparison, we added in our study another previously characterized *act-2* knock-out (KO) strain (allele *ok1229*) obtained via an EMS screen, which harbours a larger deletion extending beyond the 3' UTR (Willis *et al.* 2006).

ACT-2 missense variants affect the general viability of *C. elegans* at different levels

We first compared the general viability of the different mutant *act-2* strains obtained at 20°C. We found that some animals carrying the two single point variants p.R147S or p.T203M developed into homozygous adults but their very few progenies were 100% lethal during embryogenesis, indicating a strong maternal effect lethal phenotype. We thus maintained these variants as heterozygous animals using the nT1 balancer (Ferguson and Horvitz 1985). Interestingly, one variant (p.G74V) was identified as lethal at both homozygous and heterozygous state. We indeed obtained a few edited surviving F1 animals after injections, some of which produced very few embryos that were 100% lethal. Sequencing of several of these F1 animals confirmed the presence of a heterozygous G74V variant in the *act-2* gene (Figure S1B). Because we were unable to maintain a stable line expressing this variant, we did not pursue its characterization. Nonetheless, another variant present at the same locus (p.G74S) was maintainable when homozygous. All other variants (p.L65V, p.T120I, p.R183W, p.R196C, p.R196H) as well as the KO *rey016, rey021* and *ok1229* were viable at a homozygous state and were thus maintained as such, although some of them had very low progeny. In conclusion, out of nine single point mutation variants generated, six could be maintained as homozygous, two as heterozygous and one was not maintainable (Figure 1D). This initial finding emphasizes the importance of these loci for development and health, and highlights the remarkable conservation of actin across species. Collectively, these observations suggest that *C. elegans* stands as a pertinent and promising model for the investigation of NMA.

act-2 gene knock-out affects reproduction and embryo viability

In order to assess how single point variants compare with gene KO, we performed a detailed analysis of phenotypes in absence of ACT-2 protein expression. We assessed both the newly CRISPR generated *act-2* KO strains (*rey016 and rey021* allele) as well as the EMS

generated strain (*ok1229* allele, (Willis et al. 2006)) (Figure 1B). We first verified if transcriptional adaptation of another actin coding gene could compensate for the loss of *act-2*, as proposed by Willis *et al*. (Willis et al. 2006). Such a transcriptional adaptation has been reported in an *act-5* variant (Serobyan et al. 2020). Therefore, we measured the expression of mRNA of all actin coding genes using single animal RT-qPCR in L4 animals devoid of embryos, which potentially affect the experimental read-out (Figure 2A) (Ly, Reid, and Snell 2015). We found that both *ok1229* and *rey021* strains show a clear absence of *act-2* mRNA, thus confirming the absence of ACT-2 protein. In contrast, *act-1* and *act-3* did show an increase compared to WT (*act-1* fold change *ok1229* = 2.5, *rey021* = 6.7; *act-3* fold change *ok1229* = 4, *rey021* = 3.6), unlike *act-4* and *act-5* which only had minor fluctuations (Figure 2A). We conclude that there is transcriptional adaptation: *act-1* and *act-3* compensating for *act-2* loss.

With respects to fertility and embryonic lethality, the *ok1229* allele was described as thermosensitive, showing embryonic lethality at 26°C but not at 15°C (Willis et al. 2006). Therefore, we monitored the brood sizes and percentage of unhatched eggs in *rey021* at different temperatures, as well as in wild-type (WT) animals and in *ok1229*. We observed a reduction in the number of eggs produced by the *ok1229* and *rey021* strain compared to the WT strain both at low and high temperatures (Figure 2B). However, we did not detect a significant decrease in embryonic development success unlike previously reported for the *ok1229* strain (Figure 2B') (Willis et al. 2006). The *rey021* KO allele exhibited an increased percentage of unhatched eggs above 50% for both temperatures (Figure 2B'). Thus, these results established a difference in the developmental success in the two genetic *act-2* KO backgrounds, the *ok1229* allele showing a milder phenotype. One hypothesis might lay in different gene compensation efficiency in the embryo but not in the L4 animals of these two genetic contexts. As brood sizes and embryonic lethality were very similar at both temperatures for the *rey021* strain, we do not suspect a temperature sensitive effect for this allele. Thus, all further experiments were performed at the standard 20°C temperature.

In order to determine if the KO allele effect was dominant or recessive, we quantified brood size and embryonic lethality from heterozygotes hermaphrodites for our two CRISPR generated strains. Generally, *act-2* KO animals were reduced compared to WT but *rey021*/+ animals showed an increase in the number of progeny compared to *rey021*/*rey021* (Figure 2C). The progeny of heterozygous *rey021/*+ and *rey016*/+ hermaphrodites showed an embryonic viability very close to that of the WT (Figure 2C'). To sum up, the *act-2* KO is severely impaired

but this phenotype can be partially suppressed in the heterozygous condition, as expected for an actin maternal loss of function.

Reproductive capacity is a quantitative readout to classify actin mutants

Assessing general animal fecundity and embryonic fitness in *C. elegans* allows for the quantitative detection of potential defects in oocyte production, embryogenesis or vulva function (Schafer 2005), three actin-dependant processes. We thus measured the number of eggs laid and hatched by single homozygous animals expressing an *act-2* variant at 20°C. A reduction in egg laying was observed for all *act-2* variants, except for the p.G74S and p.R183W variant strains, which appeared unaffected (Figure 3A). The most severe reductions in fecundity were observed for the p.R147S and p.T203M missense variants (mean number of eggs laid: p.R147S = 2.3, p.T203M = 31.0, WT = 270.1), surpassing the reduction seen in the *act-2* KO condition (*rey021*=78) and partially rescued in the heterozygous condition (Figure S3A). All other missense variants showed a fecundity reduction less pronounced than the KO animals.

Consistently, the number of unhatched eggs varied significantly among actin variants with trends similar to that of fecundity (Figure 3B). The p.R147S and p.T203M variants exhibited 100% embryonic lethality if homozygous (Figure 3B) and respectively 72.7% and 58.3% if heterozygous, thus stronger than the homozygous and heterozygous *act-2* gene KO (respectively 39.75 and 16%, Figure S3B). This indicates that a high percentage of heterozygotes p.R147S and p.T203M embryos die before hatching. The p.L65V missense variant also showed significant embryonic developmental issues, with an average of 33.2% embryonic lethality and notable variability. The p.R196H variant was significantly affected, more so than the p.R196C variant, as showed by none overlapping 95% credibility intervals of the posterior distributions of the embryonic lethality rates calculated with Bayesian methods (Figure 3B). All other analysed missense variants displayed milder impairment of embryogenesis success. Taken together, our data suggest that p.R147S and p.T203M are dominant negative, p.G74S and p.R183W are not impaired in their reproductive capacity, whereas the other studied variants behave as partial loss of function alleles, with variability compared to WT.

Gonad internal architecture is impaired in selected mutants

As we observed an impairment in the reproductive capacity of the actin mutant strains, we investigated whether these defects were associated with abnormal organization in the *C. elegans* reproductive system. We thus performed a detailed analysis of gonad morphology by spinning-disk confocal microscopy using strains expressing both an actin filament probe (mex5p::Lifeact::mKate2), and endogenously labelled non-muscle myosin molecular motors (NMY-2::GFP). *C. elegans* adult hermaphrodites possess two syncytial mirror gonads shaped by highly organized actin structures. These structures include a connected cytoplasm-filled core, called the rachis, surrounded by germ cells with openings facing the rachis and shaped by stable actomyosin rings (Figure 3C). These rings are originating from incomplete cytokinesis of primordial germ cells forming the typical specific honeycomb architecture in the functional adult gonad (Bauer et al. 2021). We first characterized the gonad morphology by measuring germ cell and rachis sizes (Figure 3D). Notably, the p.L65V variant strikingly presented lower values, p.T203M showed a more moderate reduction. Interestingly the variant p.G74S presented higher rachis/gonad ratio than the control even though this is not correlated with a perturbation of fertility. Other variants had values more similar to the WT strain but exhibited greater variability. Second, we quantified defects using established criteria (Green et al. 2011) (Figure 3E). In correlation with the strong decrease of rachis size, the most pronounced phenotypes are found in the p.L65V animals, notably illustrated by the presence of 80% of degenerated gonads devoid of oocytes or early embryos. This suggests severe impairment in gonad morphogenesis and/or maintenance in these animals. Still, the penetrance was not 100% as 1/5 p.L65V animals harboured a normal looking gonad, which explains the viability of the strain. Other noticeable phenotypes present in animals expressing different point mutation were: the presence of 20% multinucleated oocytes in p.T203M animals as well as a 11% penetrance in p.T120I, multinucleated germ cells in p.T203M (100%), p.T120I (33%) and p.G74V (25%). To conclude, two main phenomena can explain a reduction in brood size in actin variant genetic backgrounds: abnormal gonad internal organization, highlighting the importance of ACT-2 for proper cytoskeleton architecture establishment in this tissue; and oocyte defects likely due to DNA segregation errors, emphasizing the importance of ACT-2 in meiosis.

ACT-2 variants affect the success rate in different embryogenesis stages

We next sought to determine causes of the observed embryonic lethality. To this end, we quantified the precise stage at which embryonic lethality occurs in the actin mutant strains (Marston and Goldstein 2006; T.K. Vuong-Brender, Yang, and Labouesse 2016) as well as the

eggshells' shapes by measuring their aspect ratios and 2D areas (Figure S3C, D). To do so, we monitored the entire duration of embryogenesis using timelapse transmitted light video-microscopy (Figure 3F). In line with the previous embryonic lethality counts, we detected a variable proportion of *act-2* mutant embryos unable to hatch (Figure 3F). Embryonic defects were categorized into various classes. First, at the zygotic stage due to a failure to complete cell division (orange in Figure 3F). Second, developmental arrest during gastrulation (yellow in Figure 3F), a key event involving cell shape changes and migration, highly dependent on Arp2/3 actin networks (Nance 2005; Zhang, Medwig-Kinney, and Goldstein 2023). Third, in the vast majority, developmental arrest occurred at later steps of development. Indeed we observed embryonic arrest during ventral enclosure (light purple in Figure 3F), a process also known to rely on both protrusive and contractile actin-related events (Bernadskaya et al. 2012). Additionally, we observed two types of arrests during elongation with Pat embryos (paralyzed at two-fold, purple in Figure 3F), suggesting muscular defective conditions and/or defective hemidesmosomes; and rupturing embryos, an obvious sign of tissue mechanics impairment (dark purple in Figure 3F) (T.K. Vuong-Brender et al. 2017). Interestingly, the total percentage of defects and their frequencies varied among the different strains but the KO condition showed a significative proportion of lethality in each category (Figure 3F). In contrast, homozygous p.R147S embryos suffered severely from early embryonic death (cytokinesis and gastrulation defects) while in heterozygous p.R147S embryos, early death was reduced, and they tended to die more frequently during ventral enclosure or in later stages of elongation. As elongation requires efficient muscle contractions, this result corroborated with p.R147S impaired muscular capacity measured in the motility assay. The few embryos expressing the p.T203M allele, arrested at different stages of morphogenesis between gastrulation and elongation with different ratios depending on the genetic condition. These findings suggest that the p.R147S and p.T203M variants are more detrimental or toxic for early embryogenesis than the complete absence of ACT-2 protein (*rey021* condition), supporting a dominant negative effect. To conclude, this analysis revealed variant-specific differences in the mechanisms leading to actin-related lethality, likely associated to a fine-tuning of specific actin organization, dynamics or mechanoproperties at these key stages of morphogenesis.

Altered cell mechanics but surprisingly mild cortical actin disorganization in early embryos

We then asked whether defects emanate from abnormal cytoskeletal organization or impaired force production, such as abnormal cytoskeletal contractility linked to actin-myosin interaction. Both possibilities are not mutually exclusive and could be linked, as architectural defects can impair contractility (Ennomani et al. 2016). We thus increased the time and scale resolution by performing spinning-disk confocal microscopy on strains carrying the LifeAct probe to follow actin filaments organization as well as an endogenously labelled non-muscle myosin (NMY-2::GFP) to assess contractility during the first cell divisions of *C. elegans (Reymann et al. 2016)*.

With respect to cortical architecture and dynamics, we were surprised by the outstandingly normal general organization of the actin networks observed in some *act-2* variants (Figure 4A), even though reduced polymerization capacities have been quantified biochemically using purified proteins (Greve and Manstein 2024). Visual inspection did not reveal major signs of impaired actin density or general organization in most embryos. Similarly, we did not detect signs of impairment in the reproducible sequence of events taking place in zygotes for most embryos. These events, which highly depend on proper cortical organization and contractility, include polarity establishment associated with cortical flows, pseudo cleavage formation, and the maintenance phase where polarity is stably maintained (Rose and Gönczy 2014). This was evidenced by the unchanged size of the daughter cell AB in variant conditions (Figure S4). Possibly many of the NMA actin variants can copolymerize with WT actin, resulting in mild phenotypes of disorganization that are compatible with life in both human and *C. elegans.*

Although most cells maintain seemingly normal actin cortical networks, we observed some cell-scale defects, revealing impaired cytoskeletal properties in some embryos (Figure 4B, C, D, E, F). As expected from previous analyses, we identified cell division defects where ingression progresses smoothly but subsequently retracts (Figure 4B). This suggests that cytokinesis ring assembly and contractility might not be impaired, but rather than failure happens at the last steps of cytokinesis completion during abscission. We also observed meiosis defects, identified by the presence of an additional nucleus present either in the AB cell or in the P0 zygote, likely due to incomplete polar body extrusion (Figure 4C). As meiosis and cytokinesis completion share common mechanical principles linked to actin, such as the formation of a contractile actin ring required to bring together closing membrane domains (Dorn et al. 2010; Flynn and McNally 2017), these failures may share a similar origin. In addition, we noticed the presence of blebs in some embryos (Figure 4D, E). Blebs are transient cell protrusions that can be triggered by two main events: the detachment of the cortex from the

plasma membrane or the formation of a crack in the cortex. Blebs then grow due to the internal hydrostatic pressure imposed by cortical contractility (Charras and Paluch 2008). Blebs were mostly observed at the 2-cell stage, at the interface between the AB and P1 cells before cell rounding prior to division. We observed larger blebs, mostly in p.L65V, p.T120I and p.T203M variants, emanating from AB, sometimes dragging the nucleus into the bleb, before a fast retraction period. Retraction coincided with the increase of myosin at the cortex at cytokinesis onset. Embryos presenting the blebbing phenotype also had transiently abnormal cell shapes, an overall less round and wavier cortical surface (Figure 4D) and seemingly altered cell-cell contacts, notably less pronounced between P1 and ABp cells at the 4-cell stage. This phenotype resembles cortical blebs that were proposed to reposition the cytokinesis ring of the zygote in the presence of *ani-1(RNAi);pig-1(gm344)* embryos in presence of excessive myosin accumulation at the anterior cortex (Pacquelet et al. 2015). While we do not observe mispositioning of the furrow or abnormal nuclei migration, the similar bleb sites suggest a general locus of cortical instability. Blebs are intrinsically linked to cortical contractility but also to cortex to membrane attachment, thus reinforcing the possibility that membrane to cortex attachment might be impaired, as suggested by late cytokinesis defects. To summarize, we showed that actin network organisation, cortical contractility and cortex to membrane attachment can be affected by the presence of actin variants but these defects are partially penetrant possibly due to a remarkable embryonic robustness to cytoskeletal perturbation.

Motility is mildly impaired for a few *act-2* variants

Like its actin cytoplasmic paralogues, ACT-2 protein is also required in muscle cells (Willis et al. 2006), as illustrated by the presence of some dominant mutations in *act-2* impacting animal motility, with uncoordinated phenotypes on 2D surfaces (Krause et al. 1989). As no such strong phenotype was observed in our studied *act-2* mutants, we quantified the animals' capacity to migrate inside a pluronic gel towards a chemoattractant (food source) in a 3D burrowing assay (Lesanpezeshki et al. 2019). We observed that 82.4% of WT animals and 50.2% of mobility-deficient control animals (*unc-2*(*gk366*)) reached the food after 2 hours (Figure 5A). We detected significantly altered migration for the KO *rey021* and for the variants p.T120I, p.R183W, p.R196C, p.R196H and p.T203M, while other variants showed unaffected migration (p.L65V, p.G74S, p.R147S). We verified that these effects were not due to impaired chemosensation (Figure S5). Note that in this assay we observed an increased proportion of immobile animals for variants *rey021* and p.T203M only. In conclusion, six out of nine assessed

act-2 variants have impaired 3D motility while two variants have a substantial population of animals defective both for 2D and 3D movement.

Low penetrance of neurogenesis defects

In human, neurodevelopmental defects are the most frequent symptoms across the whole NMA spectrum (Figure 1C). We thus studied neurons in *C. elegans* L4 animals. To this aim, we took advantage of a multicolour neuronal labelling transgene present in the NeuroPAL strain (Yemini et al. 2021). The NeuroPAL transgene encodes for the expression of a combination of 41 neuron specific reporters for gene expression and neuronal activity, associated with four different fluorophores. This labelling allows each neuron in the animal to be identified by a unique set of fluorophores, distinguishing them from neighbouring neurons. After introducing the NeuroPAL transgene in the actin variant strains, we mapped all neurons present in the animal's midbody and tail, which comprise every type of neuron. In all observed animals, we did not detect altered neuronal positions. However, we did observe rare events such as the presence of an extra numerary neuron (adjacent to SDQR or in the lumbar ganglion) or a missing neuron (such as DVB or PDA, Figure 5B). SDQ neurons are born from an asymmetric division followed by the death of their sister cell while DVB and PDA are born from the transdifferentiation of a rectal epithelial cell (Riva et al. 2022). Even if low penetrance is observed in these cases, these numbers are significative due to the extreme robustness of *C. elegans* lineage, 100% success in wild type conditions (Chai et al. 2022; Riva et al. 2022). These findings suggest a potential weakness in the process of neuronal asymmetric division or fate acquisition, which might be amplified in the context of human cortical development where asymmetric divisions have been reported in the striatum.

Data integration to build a comparative tool

Taking advantage of the multiscale characterization performed on each mutant, our final goal was to classify the different missense variants in terms of severity. We used each of the quantitative results as variables to create a Principal Component Analysis (PCA) graphical representation (Figure 6, Variables available in Figure S6). This dimension reduction allowed us to group phenotypes into different classes and allowed us to identify the few most promising variables to be used for classification purposes (Figure S6). In the PCA plot, the WT strain is located in the top left quadrant close to the mildly affected variants, defining class I (p.L65V,

p.G74S, p.T120I, p.R183W, p.R196C, p.R196H). One can note the singular position of the p.L65V, isolated in the class I group, underlying that the in-depth analysis points towards more severe consequences for this variant. This result correlates with human data, where an *ACTB* p.L65V patient presented severe symptoms and early death. The KO *rey021* strain is also isolated in a more central position. Stronger phenotypes such as in p.R147S or p.T203M variants are positioned in the right half, defining the class II. Interestingly, heterozygous variants (*rey021*/+, p.R147S/nT1 and p.T203M/nT1*)* are placed closer to the WT point than their homozygous counterpart. This correlates with human related data: several *ACTB* p.R147 patients were identified only as post-zygotic mutations, thus expressed as mosaics in a subset of epithelial cells suggesting a lethality issue in human if expressed in all cells. Several patients with variant p.T203M in *ACTG1* suffer from severe BWCFF symptoms including microcephaly, profound intellectual disability and non-ambulance. This locus is in fact a hot spot for *ACTG1* but no patient for *ACTB* has been identified so far, raising the question of lethality for *ACTB* in humans. Similarly, the *C. elegans* variant p.G74V showed 100% lethality -for which no other quantitative data can be retrieved, thus manually positioned further away on the right axis in a class III. In agreement, patients with p.G74V variant in *ACTG1* are severely affected, while no *ACTB* p.G74V variant has been discovered so far. To conclude, the severity of this initial set of *C. elegans* mutants correlates with that reported in human patients. Using quantitative multiscale analysis of a panel of actin variants, we have provided access to a valuable comparative tool enabling the positioning of newly identified variants on a graded map of survival potential if those would be similarly be reproduced in the *C. elegans* model and assessed.

III. Discussion

Patients affected by the rare disorders from the Non-Muscle Actinopathies (NMA) spectrum and its subclass BWCFF, exhibit a large range of symptoms and diverse survival potential, leading to complicated medical prognostics. In this study, we used the fast-growing and simple model organism *C. elegans* to study *in vivo* the quantitative impact of some of the associated single cytoplasmic actin variants. This choice combined many advantages including among others: an ethical choice with respect to “Replacement” strategies (3R rule), fast developmental pace, large cohorts, ease of genetics and fully transparent animals. Using CRISPR/Cas9

genome editing, we successfully generated new *C. elegans* models expressing endogenously either *de novo* actin variants identified in human patients or premature STOP mutations to reproduce loss-of-function conditions. For each variant, we quantified general fitness, reproductive capacities, muscle-based motility, embryonic development, and neuronal differentiation. If some correlations between phenotypes were observed, it is important to note that some variants showed more or less differences compared to the WT reference for each of the experiments performed (e.g., minimal embryonic lethality but impaired 3D animal motility or variations of neuronal cell number). Given the ubiquitous nature of actin, involved in numerous cellular events at all stages of development and throughout the animal lifespan, these results underly the importance of analysing multiple parameters in animal models. Parameters which should span diverse length scales: from macroscopic actin organisation to cell behaviours and phenotypes at the organism scale, in order to effectively distinguish the impact of each actin variant. The final step using an integrated PCA analysis enabled us to summarize the phenotypic classification providing a valuable tool to position newly identified variants of unknown significance on an existing map. With commercial gene editing services in *C. elegans* offering quick delivery times and automated analysis of various criteria, it is plausible that *C. elegans* NMA models, along with this new tool, could be used in the future as indicators to aid in medical prenatal diagnostics for humans.

In the functional characterization of *act-2*, a key finding is the significant phenotypic difference between our newly generated CRISPR *act-2* knock-out strains and the only previously available KO strain. Although we cannot explain the reason of such difference, our work clearly indicates that *act-2* gene KO can impact embryonic development success considerably at all temperatures. As hypothesized for human loss of function of cytoplasmic actin (Cuvertino et al. 2017), *C. elegans* also showed transcriptional adaptation to compensate *act-2* loss, as the closely related actin paralogue genes *act-1* and *act-3* were found to be upregulated. Another significant finding was that three actin variants exhibited stronger phenotypes than the *rey021 act-2* KO: p.G74V, p.T203M and p.R147S. The p.G74V variant lead to an animal producing 100% lethal embryo even as heterozygote, while embryos from variants p.T203M and p.R147S are 100% lethal only when the mother is homozygote. The latter mutations behaved as semi-dominant since these phenotypes were only partially improved in heterozygotes. This suggests that the presence of these mutated actin proteins disrupts proper function, either through essential perturbations of actin filament assembly or interactions with actin-binding proteins. This insight into allele behaviour, distinguishing dominant negative from loss-of-function variants provides valuable information that would not have been obtained if not

using *in vivo* animal models. We thus propose that variants p.G74V, p.R147S and p.T203M act as dominant negative alleles, while all other studied actin variants in this work fall in the loss of function category.

Using these models, we observed an unexpected striking difference between two substitutions at the same locus. Animals expressing the p.G74S variant show only mild effects on embryogenesis viability whereas the p.G74V animals are significantly more affected, as mentioned above. This position is of particular interest because of the neighbouring His73 which is known to undergo irreversible methylation, regulating actin's interdomain flexibility in multiple species and known to affect smooth muscle contraction in mice for example (Wilkinson et al. 2019). Additionally, due to its location within the nucleotide-binding cleft, this variant might impact the phosphate release following actin monomer incorporation into the filament. Consequently, the binding of ADF/cofilin would be perturbed, leading to impaired disassembly kinetics. Of note, *C. elegans'* ADF/cofilin homologue UNC-60 induces lethality when knocked down (K. Ono 2003). Biochemical analysis and *in vitro* studies using purified actin variants would be required to confirm these hypotheses and compare biochemically if the presence of the hydrophobic Valine is more detrimental than Serine. However, our findings underscore the importance of using *in vivo* models to understand the complexities and subtleties at play in biological organisms in the presence of actin variants.

Additionally, from a more fundamental perspective, characterizing actin variants is also powerful to identify new amino acid positions within the cytoplasmic actin that are crucial for successful embryogenesis but also to reveal new actin networks properties. For instance, we identified that variant p.L65V to be highly perturbing gonad cytoskeleton organisation and meiosis; p.R147S possibly impairing mostly branched actin networks essential at different morphogenesis stages; and p.T203M, as well as to a milder extend p.T120I and p.R196C/H, impacting rather contractility as indicated by blebbing, paralysed arrest and impaired motility. As we have demonstrated that developmental arrest at critical embryonic stages occurs at varying frequencies depending on the variant, or that p.R147S allele's homozygous lethality was linked to increased early embryonic death, contrasting with the higher late-stage lethality in heterozygous embryos, we propose that these key developmental stages act as specific "barriers" to developmental success. Barriers of different difficulty linked to the precise site of mutation, that must be successively overcome during embryogenesis. As developmental timings were not drastically affected (Hall, D.H., Herndon, L.A., and Altun, Z. 2017), we suspect that these barriers might have a biomechanical origin (Figure S3C).

Observed defects are partially penetrant and the general organization of actin at a macroscopic scale is often remarkably unaffected. This suggests an adaptation of cytoskeletal actin to perturbations, possibly originating from the cell's ability to maintain the adequate large-scale physical properties of the cortex, also known as “morphogenetic degeneracies in the actomyosin cortex” (Naganathan et al. 2018). Compensation mechanisms may ensure the robustness of embryo development by maintaining proper cytoskeleton mechanical properties. Note that a similar robustness to cytoskeleton perturbation, in that case a resistance to microtubule disassembly, was observed in the context of *C. elegans* embryonic elongation (Priess and Hirsh 1986; Quintin et al. 2018). In our context, this could also be explained by a functional compensation by other actin isotypes expressed in early embryogenesis, notably ACT-1 or ACT-3 (Willis et al. 2006), which might compensate for polymerization defects. *In vitro* experiments with purified proteins using mixtures of WT and mutant such as for p.R196H, also show a partial rescue of polymerization defects (Greve and Manstein 2024). Thus, biological variations such as gene expression fluctuation, gene compensation, actin binding protein relative concentrations, mechanochemical feedback or fluctuation of properties impacting cell or tissue mechanics, determine the embryogenesis success of each individual. Consequently, each embryo may respond differently to these compensation mechanisms and might arrest at a different developmental stage.

Finally, the initial investigation of the consequences of actin perturbation on neurogenesis revealed a weakness in acquiring the correct number of neurons, albeit not penetrant. Some identified missing or extra-numerary neurons are linked to asymmetric division and programmed cell death. The asymmetric divisions required for neuronal fate acquisition can depend on the asymmetry of Arp2/3 nucleated cortical actin polymerisation (Chai et al. 2022). As both actin polymerisation and Arp2/3 nucleation were already described to be impaired for some variants studied *in vitro* (Greve and Manstein 2024), this result is not surprising and will require further investigation in *C. elegans*. It may lead to essential findings in the path to identify the molecular to functional mechanisms at the origin of NMA neuronal pathophysiology. Importantly, the NeuroPAL data using nuclei as proxy of neuronal cell positioning, did not reveal other gross defects in terms of cell migration. This might come from the redundancy at work during development that is ensuring the robustness of final neuronal positioning in *C. elegans*. Assessing migration dynamics and axonal networks may uncover additional abnormalities not visible in the current analysis.

Altogether, this work provides a new animal model library for the study of actin variants associated with NMA. We show that different non-synonymous mutations in nematodes lead to a broad range of phenotypes as in human, and that the severity of *C. elegans* phenotypes correlates with patients' survival potential. All the tools generated here could be used to investigate the mechanisms underlying NMA pathophysiology and to screen for therapeutic strategies in the future.

IV. Methods

4.1. *C. elegans* handling :

Animals were cultured on Nematode Growth Medium plates seeded with OP50 at 20°C unless otherwise stated (Brenner 1974). Bristol strain (N2) was used as a reference. We thank the Caenorhabditis Genetics Center for providing the strains N2, DW101 and EU1383. Complete list of strains used and their genotype are available in Table 3. All novel actin variants models were generated in the Reymann lab except two, which were outsourced to Suny Biotech® (recognisable by the allele prefix syb).

4.2. *C. elegans* generation :

We performed *dpy-10* co-CRISPR edition using purified homemade Cas9 protein, synthetic tracrRNA and ssODN from IDT, as described in Paix *et al* (Paix et al. 2015). Table of crRNA and repair template used are listed in Table 1. Additional silent mutations were introduced either to add or remove a restriction enzyme recognition site for genotyping strategies as well as mutate PAM or nucleotides within the sg guides. All generated strains were then outcrossed 4 times with N2 and all actin coding genes were sequenced to verify that only *act-2* was mutated (primers list Table 2). Sequencing was performed by Eurofins®. Results are analysed using SnapGene®. The *rey016* allele consists of an insertion-deletion in exon 2 (33bp insertion + 816bp deletion) resulting in a frameshift and a premature STOP codon at the amino acid 70. The *rey021* allele presents a 35bp insertion causing a frameshift and a premature STOP codon at the amino acid 120. The *ok1229* harbours a large deletion starting at the 213th amino acid and extending beyond the 3' UTR

Note that *C. elegans'* actin including *act-2* possess an additional cysteine after the initial methionine in N-terminus compared to Human ACTB and ACTG1 (*ACTB* being MDDDIAA and *act-2* M**C**DDDVAA, Figure Sup 1A). For simplicity and easier reference to patient's variation, in order to be in frame with human numbering, we will hereafter refer to the mutations' loci by omitting this additional cysteine. For example, human variation ACTB p.L65V will be referred to as act-2 p.L65V instead of *act-2* p.L66V.

Table 1: List of guides and repair template sequences

Mutation and allele name	crRNA	Repair	Enzyme used for Genotyping
p.L65V, *rey012*	CAAUUGGGUACUUAAGGGUA	Ggtaaattttcaaaaaattt g acc gat tgg aaa tag ttg ttt tta ggt A**TC** **G**T<u>C ACT CTT AAA TAC CCA ATT G</u>AG CAT GGT ATC G	BfuI
p.G74S, *rey022*	CGUUACCAACUGGGACGACA	CTT ACC CTT AAG TAC CCA ATT GAG CAT AGT ATC GTG ACA AAT TGG GAT GAC A**TG G**AA AAA ATC TGG CAT CAC	BsmF1
p.G74V	AGCAUGGUAUCGUUACCAAC	g ttt tta gGT ATC CTT ACC CTT AAG TAC CCA ATT GAA CAT GTT ATT GTC ACT AAC **TGG** GAC GAC ATG GAA AAA ATC TGG C	PciI
p.T120I, *rey014*	AUACAUGGCUGGGGUAUUGA	CT AAC CGT GAA AAG ATG ATC CAA ATC ATG TTC GAG **ACA** TTC AAT ACA CCA GCA ATG TAC GTC GCC ATC CAA GCT G	BsaBI
p.R147S, *syb3920*	NA.	CAA GCT GTC CTC TCC CTC TAC GCT TCC GGG TCG ACC ACG GGA ATC GTC CTC GAC TCT GGA GAT	AccI
p.R183W, *syb5567*	NA.	ACG CAC ACA GTC CCA ATC TAC GAA GGA TAT GCC CTC CCA CAC GCC ATC CTC CGT CTT GAC TTG GCC GGA TGG GAT CTT ACT GAT TAC CTC ATG AAG ATC CTT ACC GAG CGT GGT TAC TCT TTC ACC ACC ACC GCT GAG CGT GAA	HaeIII

		ATC GTC CGT GAC ATC AAG GAG AAG CTT TGT TAC GTC GCG	
p.R196C, *syb3909*	NA.	GGA ATC GTC CTC GAC TCT GGA GAT GGT GTT ACG CAC ACA GTC CCA ATC TAC GAA GGA TAT GCC CTC CCA CAC GCC ATC CTC CGT CTT GAC TTG GCT GGA CGT GAT CTT ACT GAT TAC CTC ATG AAG ATC TTG ACC GAA TGC GGT TAC TCT TTC ACC ACC ACC GCT GAG CGT GAA ATC GTC CGT GAC ATC AAG GAG AAG CTT TGT TAC GTC GCG CTC GAT TTC GAG CAA GAA ATG GCC ACC GCC	BglII
p.R196H, *rey020*	AUGAAGAUCCUUACCGAGCG	CTT ACT GAT TAC CTC ATG AAA ATT CTT ACC GAG CA**T GG**T TAC TCT TTC ACC ACC ACC GCT GAG CGT GAA ATC	AlWI
p.T203M, *rey023*	GACGAUUUCACGCUCAGCGG	G AAG ATC CTT ACC GAG CGT GGT TAC TCT TTC ACC **ACT** ATG GCA GAG CGA GAA ATT GTG CGT GAC ATC AAG GAG	MspAII
KO, *rey021*	AGCAUGGUAUCGUUACCAAC	NA.	
KO, *rey016*	AUACAUGGCUGGGGUAUUGA	NA.	

Legend : Lower case (non-coding), upper case (coding), red (silent mutation), blue (non-synonymous mutation of interest), bold (PAM sequence), underlined (crRNA sequence)

Table 2: List of PCR primers used

Gene	Forward primer	Reverse primer	Hybridization temperature	Amplicon length
act-1	oAC064 ttccccacgtgttctgtg	oAC056 GTTTGTGCAAGTTGACG AAG	54°C	1323pb
act-2	oAC070 CTCGTAGTTGACAATGGA TC	oAC069 CCAACAGTGATGACTTG TCCG	56°C	776pb
act-2	oAC043 gctggtttaattggaaagct	oAC052 gtcagccagttcaccacgaa	55°C	2544pb
act-3	oAC065 ccttcccacacccacttg	oAC066 gggaccataacgatttggtg	60°C	1495pb
act-4	oAC067	oAC068	50°C	1379pb

	ctcgaccgaattctcgcc	ggttgcgggataatacgaac		
act-5	oAC061 CGTTTTCTATAAACTCGACTTC	oAC062 GAAATGGAAGGCACATGT	51°C	1500pb

Table 3: List of strain used for this study

Name	Genotype	From
ACR061	*act-2* (*rey012* [Leu65Val]) V	This study
ACR096	*nmy-2*(*cp7*[*nmy-2*::gfp + LoxP *unc-119*(+) LoxP]) I; *gesIs001* ([*mex-5*p::Lifeact::mKate::*nmy-2*UTR, *unc-119* (+)]) ; *unc119*(*ed3*) III; *act-2* (*rey012* [Leu65Val]) V	This study
ACR153	*otIs696* ; *act-2* (*rey012* [Leu65Val]) V	This study
ACR108	*act-2* (*rey022* [Gly74Ser]) V	This study
ACR224	*nmy-2*(*cp7*[*nmy-2*::gfp + LoxP *unc-119*(+) LoxP]) I; *gesIs001* ([*mex-5*p::Lifeact::mKate::*nmy-2*UTR, *unc-119* (+)]) ; *unc119*(*ed3*) III; *act-2* (*rey022* [Gly74Ser]) V	This study
ACR165	*otIs696* ; *act-2* (*rey022* [Gly74Ser]) V	This study
ACR070	*act-2* (*rey014* [Thr120Ile]) V	This study
ACR139	*nmy-2*(*cp7*[*nmy-2*::gfp + LoxP *unc-119*(+) LoxP]) I; *gesIs001* ([*mex-5*p::Lifeact::mKate::*nmy-2*UTR, *unc-119* (+)]) ; *unc119*(*ed3*) III; *act-2* (rey014 [Thr120Ile]) V	This study
ACR137	*otIs696* ; *act-2* (*rey014* [Thr120Ile]) V	This study
ACR168	*act-2*(*syb3920*[Arg147Ser]/nT1[*qIs51*]) V	This study
ACR216	*otIs696* ; *act-2*(*syb3920*[Arg147Ser]/nT1[*qIs51*]) V	This study
PHX5567	*act-2* (*syb5567* [Arg183Thr]) V	This study
ACR125	*act-2* (*syb3909*[Arg196Cys]) V	This study
ACR135	*nmy-2*(*cp7*[*nmy-2*::gfp + LoxP *unc-119*(+) LoxP]) I; *gesIs001* ([*mex-5*p::Lifeact::mKate::*nmy-2*UTR, *unc-119* (+)]) ; *unc119*(*ed3*) III; *act-2* (*syb3909*[Arg196Cys]) V	This study
ACR166	*otIs696* ; *act-2* (*syb3909*[Arg196Cys]) V	This study

ACR085	*act-2* (*rey020* [Arg196His]) V	This study
ACR107	*nmy-2*(*cp7*[*nmy-2*::gfp + LoxP *unc-119*(+) LoxP]) I; *gesIs001* ([*mex-5*p::Lifeact::mKate::*nmy-2*UTR, *unc-119* (+)]) ; *unc119*(*ed3*) III; *act-2* (*rey020* [Arg196His]) V	This study
ACR136	*otIs696* ; *act-2*(*rey020*[Arg196His]) V	This study
ACR099	*act-2*(*rey023*[Thr203Met]) / DnT1[*qIs50*] (IV;V)	This study
ACR122	*gesIs001* ([*mex-5*p::Lifeact::mKate::*nmy-2*UTR, *unc-119* (+)]) ; *unc119*(*ed3*) III; *act-2*(*rey023* [Thr203Met]) / DnT1[*qIs50*] (IV;V)	This study
ACR219	*otIs696* ; *act-2*(*rey023*[Thr203Met]) / DnT1[*qIs50*] (IV;V)	This study
EU1383/ACR162	*act-2*(*ok1229*) V	Willis et al., 2006
ACR161	*act-2* (*rey016*(KO)) V	This study
ACR149	*act-2* (*rey021*(KO)) V	This study
ACR173	*otIs696* ; *act-2*(*rey021*[KO]) V	This study
DW101	*atl-1*(*tm853*) V/ DnT1[*qIs50*] (IV;V)	S. Mitani
VC854	*unc-2*(*gk366*) X	The C. elegans Deletion Mutant Consortium, 2012
SWG007	*nmy-2*(*cp7*[*nmy-2*::gfp + LoxP *unc-119*(+) LoxP]) I; *gesIs001* ([*mex-5*p::Lifeact::mKate::*nmy-2*UTR, *unc-119* (+)]) ; *unc119*(*ed3*) III	Reymann et al., 2016
OH15495	*otIs696*	Yemini et al., 2021
N2	Wild-type	Brenner, 1974

4.3. Phenotypic characterization:

4.3.1. Egg-laying assay

Total brood size of single hermaphrodites was quantified, by transferring single L4 animals from well to well every day on 6 well plates. Eggs from the previous day are counted. 36-48 hours after, the number of larvae is counted to determine the hatching percentage. Plates were maintained at the desired temperature (15°C or 20°C or 25°C) and checked for any contamination or lethality of the P0 hermaphrodite, in which case the animal was discarded from

analysis. Note that heterozygotes *act-2* KO *rey016*/+ and *rey021*/+ (Figure 2C) were assessed in non-balanced nT1 background. We verified the animals' genotype by sequencing their progeny after experiment completion.

4.3.2. Motility burrowing assay

We followed Lesanpezeshki et al. protocol (Lesanpezeshki et al. 2019) and Ana Carvalho optimisation (personal communication). Liquid Pluronic gel (F-127 Pluronic from Sigma, dilution at 4 degrees of 13g in 37mL water) and all consumables were maintained at 10 degrees prior use. Height of gel was 0.6µm. Concentrated (100mg/mL) OP50 was use as chemoattractant. The negative control, *unc-2*(gk366) is a KO of the ortholog of human CACNA1B (calcium voltage-gated channel subunit alpha1 B), thus predicted to enable high voltage-gated calcium channel activity expressed in whole body wall muscle and required for proper animal motility. We used standard chemosensation assay where staged young adults were washed 4 times and placed at the center of an empty plate. Concentrated (100mg/mL) OP50 and Ultra Pure H_20 were placed on opposite extremities of the plate. After one hour, the number of animals on each side of the plates were counted as well as the animals that did not move from their original positions ("Immobile animals" in Figure S2C). Chemotaxis index was calculated using $I = \frac{n_{OP50} - n_{H_2O}}{n_{Total} - n_{immobile\ animals}}$.

4.4. RT-qPCR :

Single animal RT-qPCR was performed with minimal changes from Ly, Reid and Snell (Ly, Reid, and Snell 2015). Briefly, a single animal was transferred to a 0.2mL Eppendorf tube without the help of bacteria into 2µL of lysis buffer (5 mM Tris-HCl pH 8.0, 0.5% Triton X-100, 0.5%, Tween 20, 0.25 mM EDTA and 1 mg/mL proteinase K). The tube was incubated at 65°C for 10 min, then at 85°C for 1min in a T100™ Thermal Cycler. After lysis completion, we used the Maxima H Minus cDNA synthesis kit. Genomic DNA was removed by adding one microliter of a master mix containing 1µL of dsDNAse buffer, 1µL of DsDNAse and 8µL of nuclease free water to one microliter of lysis product. The solution was incubated at 37°C for 2 minutes and immediately chilled on ice. cDNA synthesis was performed by placing one microliter of cDNA synthesis mix to the lysate. We then generated cDNA by adding one µL of a mix containing 0.5µL oligo dT primer, 0.5µL 10mM dNTP, 6.5µL nuclease free water, 2µL RT buffer and 0.5µL Maxima H Minus enzyme mix. We centrifuged our tubes and incubated it at 25°C for 10 minutes, then at 55°C for 30 minutes then 5 minutes at 85°C. We diluted the cDNA to 25 µL with nuclease free water and used it immediately. We used a LightCycler® for qPCR. We used the

Lightcycler® 480 SYBR Green | Master mix and followed its protocol thoroughly. Primers used for amplification are (all in 5' -> 3' ; hybridization temperature = 54°C) *act-1* (Forward : GCCCCATCAACCATGAAG, Reverse : gtttgtgcaagttgacgaag), *act-2* (Forward : CTCGTAGTTGACAATGGATC, Reverse : CCTCTCTTGGATTGGGCC), *act-3* (Forward : GCCCCATCAACCATGAAG, Reverse : ggtaaggcgaagagcTTAGA), *act-4* (Forward : ATCGATTGTCCACCGCAAG, Reverse : ggttgcgggataatacgaac), *act-5* (Forward : GCTCCAAGCACAATGAAG, Reverse : gaaatggaaggcacatgt), *iscu-1* (Forward : GAAGGTTATCGATCACTACGAG, Reverse : CGTTATCGTCGACTCGAATC). *iscu-1* was used as a reference gene (Hoogewijs et al. 2008; Ly, Reid, and Snell 2015). Primer pairs efficiencies were measured using standard curve (Figure S2A).

4.5. Microscopy :

4.5.1. Embryonic development timelapses

L4 animals were put on a plate at 20°C 24h before acquisition. To obtain embryos, dissections were realised on a slide covered with an Idylle® 9 well Stencell (Pasturel, Strale, and Studer 2020) with 5µL of M9 and 4 animals of the desired genotype in each well (Pasturel, Strale, and Studer 2020). Then, corpses were removed from each well using a mouth micropipette. The slide containing the dissected animals was then sticked to a #1.5 coverslip (Marienfeld Superior) and placed on a Zeiss Axio-Observer 7. DIC images were then acquired using a Hamamatsu orca flash 4.0 LT camera, every 10 second for 40 minutes and then every 10 minutes for at least 14 hours with a 20x/0.8 PLAN-Apochromat objective.

4.5.2. Early embryogenesis

L4 animals were put on a plate at 20°C 24 hours before acquisition. Dissection of 5 animals was realised in 5µL of M9. The slide containing the dissected animals was then sticked to a 2% agarose pad and placed on an inverted microscope Nikon EclipseTi-2 equipped with YOKOGAWA CSU X1 spinning disk head. Pictures were then acquired using a Photometrics Prime 95B camera each 2 or 10 second for 15 minutes with a plan apo 100x/1.45 Nikon objective.

4.5.3. Gonad imaging

L4 animals were placed in 10uL of 1mM Levamisole and placed on a 2% agarose pad. Acquisition of gonads were done one a LEICA DMI8 inverted microscope equipped with Yokogawa CSU W1 Spinning disk. Z-stacks were acquired using a Hamamatsu Orca Flash 4.0

camera with a 40X HCX PL APO oil immersion objective with a 0.2µm Z-step. Gonads widths were measured using FIJI by drawing a line with a 120-pixel width across the gonads germs cells and rachis in front of the +1 oocyte. Classification of phenotypes was done visually as represented in Green et al., 2011(Green et al. 2011). Heatmap was built using the heatmap.2 function from R package gplots. The mean number of observed phenotypes for each variable were scaled in the row direction.

4.5.4. NeuroPal

L4 animals were placed in 7µL of 125mM sodium azide and placed on a 2% agarose pad. Acquisitions were done accordingly to https://www.hobertlab.org/wp-content/uploads/2019/09/Configuring-Your-Microscope-for-NeuroPAL-v2.pdf on a Confocal Inverted Leica TCS SP8X equipped with DMI6000 microscope White Light Laser using an 40x/1.3 HC PL APO CS oil immersion objective with a distance of 0.9µm between each Z. Mapping and comparison of the expected expression pattern is performed using the published tools and reference atlas map.

2.6 *In silico* analysis

The primary sequence of ACT-2 from *C. elegans* was obtained from the UniProt database (ID: P10984). We used Alphafold2 (Jumper et al. 2021) to predict the structure of ACT-2 G-actin. Calculations were performed on the Halime HPC cluster at the Institute for Biophysical Chemistry at Hannover Medical School. We visualized ATP in the nucleotide binding cleft of ACT-2 G-actin by aligning the predicted ACT-2 structure with the structure of bovine ATP-bound G-actin (PDB-ID: 2BTF, (Schutt et al. 1993)). The homology model of the ACT-2 filament was generated using the SWISS-MODEL server (Waterhouse et al. 2018) with the ADP-bound human cytoskeletal β-actin filament (PDB-ID: 8DNH, (Arora et al. 2023) as a template. ChimeraX (Pettersen et al. 2021) was used for visualization of the structures and assessment of the potential implications of the variants for actin structure.

2.7 Data analysis, visualisation and statistics

We used R 4.4.1 through R-Studio 2023.12.1 and JAGS for all data analysis with all the required additional packages in their latest version available. Codes are available on our lab github. The statistical analysis were performed in the frame of Bayesian methods. The experimental data was enriched within the Bayesian framework by inference based on posterior distribution description. For embryonic lethality: Poisson distribution was used to estimate the

embryonic lethality rates using an offset to take into account the dependency with the number of eggs laid per animal (brood size) and specific parameters values for each genotype. Parameters were either given informative Normal priors: considering a very small lethality rate for WT N(0.01, 0.1), more probable lethality for all mutants N(0.1, 0.1) except the KO homozygotes for which we estimated a possible lethality of half the embryos N(0.5, 0.1). The analysis was also computed using low informative priors for all genotypes N(0,0.01) and gave similar results within a thousandth. Note that the observed 100% embryonic lethal genotypes were not included in the model. The posterior distribution was computed using the Markov chain Monte Carlo method (McMC). A burn-in of 2000 iterations, followed by 50000 iterations was used for each of the 3 McMC chains, yielding a final 28800 iterations-sample for retrieving posterior distribution characteristics. Convergence of the McMC sample chains was checked graphically. Convergence was observed in each case. For each analysis on the main outcome, we computed the 95% credible interval of the embryonic failure rates for each genotype.

For the 3D motility assay, we compared the observed success rated to reach the chemoattractant after 2h by calculating their respective posterior distributions using two binomial distributions. We used the following priors : for WT mean = 0.9, sd=0.1 thus a probability modelled as p~dbeta(7.2, 0.8) and for all mutants a mean=0.5, sd=0.2 thus a probability modelled as p~dbeta(2.65, 2.65). A burn-in of 5000 iterations, followed by 105000 iterations was used for the McMC chain, in order to retrieve the posterior distributions. The odds ratio (OR), an estimation of the multiplication of the risk to fail reaching the target compared to WT, as well as the probability (p) that the difference between the two mean posterior probabilities is superior to 0.2 are indicated.

Acknowledgments

We would like to particularly thank the Imaging Center of IGBMC (ici.igbmc.fr) with the assistance of Elvire Guiot, Erwan Grandgirard, Yves Lutz and Bertrand Vernay. We warmly thank Dietmar Manstein (D.J.M) for his significant contributions to the project design and throughout grant application procedures. We also thank Juliette Godin, Sophie Quintin and Michel Labouesse for critical reading of the manuscript. Thanks to Robert W. Fernandez post

doc from Oliver Hobert's lab for training us to NeuroPAL as well as to our junior visitor scientists Fanny Bouvier, Emil Zessin and Johann Marois for their help.

Funding

This work was funded by European Joint Program for Rare Diseases through the European Union's Horizon 2020 research and innovation program under the EJP RD COFUND–EJP N° 825575. N.D.D. and D.J.M./J.N.G. with support from the German Federal Ministry of Education and Research under Grant Agreements 01GM1922A and 01GM1922B, respectively. A-C.R. under the project ANR-19-RAR4-0001-03. A-C.R. was also supported by the French Fondation Maladies Rares under the project SAM-2022-121409. This work of the Interdisciplinary Thematic Institute IMCBio+, as part of the ITI 2021-2028 program of the University of Strasbourg, CNRS and Inserm, was supported by IdEx Unistra (ANR-10-IDEX-0002), and by SFRI-STRAT'US project (ANR-20-SFRI-0012) and EUR IMCBio (ANR-17-EURE-0023) under the framework of the France 2030 Program. N.D.D received grant support from Deutsche Forschungsgemeischaft (DFG) (DI 2170/3-1 and DI 2170/5-1), Else-Kröner-Fresenius Stiftung (2020_EKES.04) and German Federal Ministry of Education and Research under Grant Agreements 01GM1922A. We acknowledge the Imaging Center of IGBMC, member of the national infrastructure France-BioImaging supported by the French National Research Agency (ANR-10-INBS-04). A-C.R. is a CNRS investigator. N.A. is an Unistra technician personnel. J.N.G. is supported by the HiLF I grant for early career researchers from Hannover Medical School. Some strains were also provided by the CGC, which is funded by NIH Office of Research Infrastructure Programs (P40 OD010440).

"The authors declare that they have no conflict of interest."

References

Arora, Amandeep S, Hsiang-Ling Huang, Ramanpreet Singh, Yoshie Narui, Andrejus Suchenko, Tomoyuki Hatano, Sarah M Heissler, Mohan K Balasubramanian, and Krishna Chinthalapudi. 2023. "Structural Insights into Actin Isoforms." Edited by Pekka Lappalainen, Anna Akhmanova, and Vitold Galkin. *eLife* 12 (February):e82015. https://doi.org/10.7554/eLife.82015.

Avery, L. 1993. "The Genetics of Feeding in Caenorhabditis Elegans." *Genetics* 133 (4): 897–917. https://doi.org/10.1093/genetics/133.4.897.

Bauer, Jack, Vincent Poupart, Eugénie Goupil, Ken C. Q. Nguyen, David H. Hall, and Jean-Claude Labbé. 2021. "The Initial Expansion of the C. Elegans Syncytial Germ Line Is Coupled to Incomplete Primordial Germ Cell Cytokinesis." *Development (Cambridge, England)* 148 (18): dev199633. https://doi.org/10.1242/dev.199633.

Bernadskaya, Yelena Y, Andre Wallace, Jillian Nguyen, William A Mohler, and Martha C Soto. 2012. "UNC-40/DCC, SAX-3/Robo, and VAB-1/Eph Polarize F-Actin during Embryonic Morphogenesis by Regulating the WAVE/SCAR Actin Nucleation Complex." Edited by Andrew D Chisholm. *PLoS Genetics* 8 (8): e1002863. https://doi.org/10.1371/journal.pgen.1002863.s003.

Blanchoin, Laurent, Rajaa Boujemaa-Paterski, Cécile Sykes, and Julie Plastino. 2014. "Actin Dynamics, Architecture, and Mechanics in Cell Motility." *Physiological Reviews* 94 (1): 235–63. https://doi.org/10.1152/physrev.00018.2013.

Boiero Sanders, Micaela, Christopher P Toret, Audrey Guillotin, Adrien Antkowiak, Thomas Vannier, Robert C Robinson, and Alphée Michelot. 2022. "Specialization of Actin Isoforms Derived from the Loss of Key Interactions with Regulatory Factors." *The EMBO Journal* 41 (5): e107982. https://doi.org/10.15252/embj.2021107982.

Brenner, S. 1974. "The Genetics of Caenorhabditis Elegans." *Genetics* 77 (1): 71–94.

Bunnell, Tina M., Brandon J. Burbach, Yoji Shimizu, and James M. Ervasti. 2011. "β-Actin Specifically Controls Cell Growth, Migration, and the G-Actin Pool." *Molecular Biology of the Cell* 22 (21): 4047–58. https://doi.org/10.1091/mbc.e11-06-0582.

Bunnell, Tina M., and James M. Ervasti. 2010. "Delayed Embryonic Development and Impaired Cell Growth and Survival in *Actg1* Null Mice." *Cytoskeleton* 67 (9): 564–72. https://doi.org/10.1002/cm.20467.

Cai, Emily D., Bryan K. Sun, Audris Chiang, Anna Rogers, Laura Bernet, Binbin Cheng, Joyce Teng, Kerri E. Rieger, and Kavita Y. Sarin. 2017. "Postzygotic Mutations in Beta-Actin Are Associated with Becker's Nevus and Becker's Nevus Syndrome." *The Journal of Investigative Dermatology* 137 (8): 1795–98. https://doi.org/10.1016/j.jid.2017.03.017.

Chacon-Camacho, Oscar F., Tania Barragán-Arévalo, Camilo E. Villarroel, Mónica Almanza-Monterrubio, and Juan Carlos Zenteno. 2020. "Previously Undescribed Phenotypic Findings and Novel *ACTG1* Gene Pathogenic Variants in Baraitser-Winter Cerebrofrontofacial Syndrome." *European Journal of Medical Genetics* 63 (5): 103877. https://doi.org/10.1016/j.ejmg.2020.103877.

Chai, Yongping, Dong Tian, Zhiwen Zhu, Yuxiang Jiang, Shanjin Huang, Dou Wu, Guangshuo Ou, and Wei Li. 2022. "Wnt Signaling Polarizes Cortical Actin Polymerization to Increase Daughter Cell Asymmetry." *Cell Discovery* 8 (1): 22. https://doi.org/10.1038/s41421-022-00376-4.

Charras, Guillaume, and Ewa Paluch. 2008. "Blebs Lead the Way: How to Migrate without Lamellipodia." *Nature Reviews. Molecular Cell Biology* 9 (9): 730–36. https://doi.org/10.1038/nrm2453.

Cianci, Paola, Grazia Fazio, Sara Casagranda, Marco Spinelli, Carmelo Rizzari, Gianni Cazzaniga, and Angelo Selicorni. 2017. "Acute Myeloid Leukemia in Baraitser–Winter

Cerebrofrontofacial Syndrome." *American Journal of Medical Genetics Part A* 173 (2): 546–49. https://doi.org/10.1002/ajmg.a.38057.

Conboy, Erin, Filippo Vairo, Darrel Waggoner, Carole Ober, Soma Das, Radhika Dhamija, Eric W. Klee, and Pavel Pichurin. 2017. "Pathogenic Variant in ACTB, p.Arg183Trp, Causes Juvenile-Onset Dystonia, Hearing Loss, and Developmental Delay without Midline Malformation." *Case Reports in Genetics* 2017:9184265. https://doi.org/10.1155/2017/9184265.

Cuvertino, Sara, Helen M Stuart, Kate E Chandler, Neil A Roberts, Ruth Armstrong, Laura Bernardini, Sanjeev Bhaskar, et al. 2017. "ACTB Loss-of-Function Mutations Result in a Pleiotropic Developmental Disorder." *The American Journal of Human Genetics* 101 (6): 1021–33.

Dominguez, Roberto, and Kenneth C. Holmes. 2011. "Actin Structure and Function." *Annual Review of Biophysics* 40 (Volume 40, 2011): 169–86. https://doi.org/10.1146/annurev-biophys-042910-155359.

Dorn, Jonas F, Li Zhang, Véronique Paradis, Daniel Edoh-Bedi, Sylvester Jusu, Paul S Maddox, and Amy Shaub Maddox. 2010. "Actomyosin Tube Formation in Polar Body Cytokinesis Requires Anillin in C. Elegans." *Current Biology* 20 (22): 2046–51.

Dugina, Vera, Ingrid Zwaenepoel, Giulio Gabbiani, Sophie Clément, and Christine Chaponnier. 2009. "β- and γ-Cytoplasmic Actins Display Distinct Distribution and Functional Diversity." *Journal of Cell Science* 122 (16): 2980–88. https://doi.org/10.1242/jcs.041970.

Eggink, Hendriekje, Martje E. van Egmond, Corien C. Verschuuren-Bemelmans, Marleen C. Schönherr, Tom J. de Koning, D.L. Marinus Oterdoom, J. Marc C. van Dijk, and Marina A.J. Tijssen. 2017. "Dystonia-Deafness Syndrome Caused by a β-Actin Gene Mutation and Response to Deep Brain Stimulation." *Movement Disorders* 32 (1): 162–65. https://doi.org/10.1002/mds.26842.

Ennomani, Hajer, Gaëlle Letort, Christophe Guérin, Jean-Louis Martiel, Wenxiang Cao, François Nédélec, Enrique M De La Cruz, Manuel Théry, and Laurent Blanchoin. 2016. "Architecture and Connectivity Govern Actin Network Contractility." *Current Biology*, February, 1–12.

Ferguson, E. L., and H. R. Horvitz. 1985. "Identification and Characterization of 22 Genes That Affect the Vulval Cell Lineages of the Nematode Caenorhabditis Elegans." *Genetics* 110 (1): 17–72. https://doi.org/10.1093/genetics/110.1.17.

Flynn, Jonathan R., and Francis J. McNally. 2017. "A Casein Kinase 1 Prevents Expulsion of the Oocyte Meiotic Spindle into a Polar Body by Regulating Cortical Contractility." *Molecular Biology of the Cell* 28 (18): 2410–19. https://doi.org/10.1091/mbc.e17-01-0056.

Freitas, Julian Letícia, Thiago Cardoso Vale, Orlando G.P. Barsottini, and José Luiz Pedroso. 2019. "Expanding the Phenotype of Dystonia-Deafness Syndrome Caused by ACTB Gene Mutation." *Movement Disorders Clinical Practice* 7 (1): 86–87. https://doi.org/10.1002/mdc3.12854.

Gearing, Marla, Jorge L. Juncos, Vincent Procaccio, Claire-Anne Gutekunst, Elaine M. Marino-Rodriguez, Kymberly A. Gyure, Shoichiro Ono, et al. 2002. "Aggregation of Actin and Cofilin in Identical Twins with Juvenile-Onset Dystonia." *Annals of Neurology* 52 (4): 465–76. https://doi.org/10.1002/ana.10319.

Green, Rebecca A., Huey-Ling Kao, Anjon Audhya, Swathi Arur, Jonathan R. Mayers, Heidi N. Fridolfsson, Monty Schulman, et al. 2011. "A High-Resolution C. Elegans Essential Gene Network Based on Phenotypic Profiling of a Complex Tissue." *Cell* 145 (3): 470–82. https://doi.org/10.1016/j.cell.2011.03.037.

Greve, Johannes N., and Dietmar J. Manstein. 2024. “Baraitser–Winter Syndrome Hotspot Mutation R196H in Cytoskeletal β–Actin Reduces F–Actin Stability and Perturbs Interaction with the Arp2/3 Complex.” https://doi.org/10.1101/2024.03.20.585892.

Greve, Johannes N., Anja Marquardt, Robin Heiringhoff, Theresia Reindl, Claudia Thiel, Nataliya Di Donato, Manuel H. Taft, and Dietmar J. Manstein. 2023. “The Non–Muscle Actinopathy–Associated Mutation E334Q in Cytoskeletal γ–Actin Perturbs Interaction of Actin Filaments with Myosin and ADF/Cofilin Family Proteins.” Preprint. https://doi.org/10.7554/eLife.93013.1.

Greve, Johannes N., Frederic V. Schwäbe, Thomas Pokrant, Jan Faix, Nataliya Di Donato, Manuel H. Taft, and Dietmar J. Manstein. 2022. “Frameshift Mutation S368fs in the Gene Encoding Cytoskeletal β-Actin Leads to ACTB-Associated Syndromic Thrombocytopenia by Impairing Actin Dynamics.” *European Journal of Cell Biology* 101 (2): 151216. https://doi.org/10.1016/j.ejcb.2022.151216.

Hall, D.H., Herndon, L.A., and Altun, Z. 2017. “Introduction to C. Elegans Embryo Anatomy.” *WormAtlas*. https://doi.org/doi:10.3908/wormatlas.4.1.

Happle, Rudolf. 2017. “Becker’s Nevus and Lethal Beta-Actin Mutations.” *Journal of Investigative Dermatology* 137 (8): 1619–21. https://doi.org/10.1016/j.jid.2017.04.003.

Hayashi, Yuriko, Kanako Ono, and Shoichiro Ono. 2019. “Mutations in Caenorhabditis Elegans Actin, Which Are Equivalent to Human Cardiomyopathy Mutations, Cause Abnormal Actin Aggregation in Nematode Striated Muscle.” *F1000Research* 8 (March):279. https://doi.org/10.12688/f1000research.18476.1.

Hoogewijs, David, Koen Houthoofd, Filip Matthijssens, Jo Vandesompele, and Jacques R Vanfleteren. 2008. “Selection and Validation of a Set of Reliable Reference Genes for Quantitative Sod Gene Expression Analysis in C. Elegans.” *BMC Molecular Biology* 9 (1): 9. https://doi.org/10.1186/1471-2199-9-9.

Jumper, John, Richard Evans, Alexander Pritzel, Tim Green, Michael Figurnov, Olaf Ronneberger, Kathryn Tunyasuvunakool, et al. 2021. “Highly Accurate Protein Structure Prediction with AlphaFold.” *Nature* 596 (7873): 583–89. https://doi.org/10.1038/s41586-021-03819-2.

Krause, Michael, Martha Wild, Brad Rosenzweig, and David Hirsh. 1989. “Wild-Type and Mutant Actin Genes in Caenorhabditis Elegans.” *Journal of Molecular Biology* 208 (3): 381–92. https://doi.org/10.1016/0022-2836(89)90503-2.

Lai, Wing-Fu, and Wing-Tak Wong. 2020. “Roles of the Actin Cytoskeleton in Aging and Age-Associated Diseases.” *Ageing Research Reviews* 58 (March):101021. https://doi.org/10.1016/j.arr.2020.101021.

Landel, C. P., M. Krause, R. H. Waterston, and D. Hirsh. 1984. “DNA Rearrangements of the Actin Gene Cluster in Caenorhabditis Elegans Accompany Reversion of Three Muscle Mutants.” *Journal of Molecular Biology* 180 (3): 497–513. https://doi.org/10.1016/0022-2836(84)90024-x.

Latham, Sharissa L., Nadja Ehmke, Patrick Y. A. Reinke, Manuel H. Taft, Dorothee Eicke, Theresia Reindl, Werner Stenzel, et al. 2018. “Variants in Exons 5 and 6 of ACTB Cause Syndromic Thrombocytopenia.” *Nature Communications* 9 (1): 4250. https://doi.org/10.1038/s41467-018-06713-0.

Lesanpezeshki, Leila, Jennifer E. Hewitt, Ricardo Laranjeiro, Adam Antebi, Monica Driscoll, Nathaniel J. Szewczyk, Jerzy Blawzdziewicz, Carla M. R. Lacerda, and Siva A. Vanapalli. 2019. “Pluronic Gel-Based Burrowing Assay for Rapid Assessment of Neuromuscular Health in C. Elegans.” *Scientific Reports* 9 (1): 15246. https://doi.org/10.1038/s41598-019-51608-9.

Ly, Kien, Suzanne J. Reid, and Russell G. Snell. 2015. “Rapid RNA Analysis of Individual Caenorhabditis Elegans.” *MethodsX* 2:59–63. https://doi.org/10.1016/j.mex.2015.02.002.

MacQueen, A. J., J. J. Baggett, N. Perumov, R. A. Bauer, T. Januszewski, L. Schriefer, and J. A. Waddle. 2005. “ACT-5 Is an Essential Caenorhabditis Elegans Actin Required for Intestinal Microvilli Formation.” *Molecular Biology of the Cell* 16 (7): 3247–59. https://doi.org/10.1091/mbc.e04-12-1061.

Markaki, Maria, and Nektarios Tavernarakis. 2010. “Modeling Human Diseases in *Caenorhabditis Elegans*.” *Biotechnology Journal* 5 (12): 1261–76. https://doi.org/10.1002/biot.201000183.

Marston, Daniel J, and Bob Goldstein. 2006. “Actin-Based Forces Driving Embryonic Morphogenesis in Caenorhabditis Elegans.” *Current Opinion in Genetics & Development* 16 (4): 392–98.

Michelot, Alphée, and David G Drubin. 2011. “Building Distinct Actin Filament Networks Review in a Common Cytoplasm.” *Current Biology* 21 (14): R560–69.

Murrell, Michael, Patrick W Oakes, Martin Lenz, and Margaret L Gardel. 2015. “Forcing Cells into Shape: The Mechanics of Actomyosin Contractility.” *Nature Publishing Group* 16 (8): 486–98.

Naganathan, Sundar Ram, Sebastian Fürthauer, Josana Rodriguez, Bruno Thomas Fievet, Frank Jülicher, Julie Ahringer, Carlo Vittorio Cannistraci, and Stephan W. Grill. 2018. “Morphogenetic Degeneracies in the Actomyosin Cortex.” *eLife* 7 (October):e37677. https://doi.org/10.7554/eLife.37677.

Nance, Jeremy. 2005. “Gastrulation in C. Elegans.” *WormBook*.

Ono, K. 2003. “Specific Requirement for Two ADF/Cofilin Isoforms in Distinct Actin-Dependent Processes in Caenorhabditis Elegans.” *Journal of Cell Science* 116 (10): 2073–85.

Ono, Shoichiro. 2014. “Regulation of Structure and Function of Sarcomeric Actin Filaments in Striated Muscle of the Nematode *Caenorhabditis Elegans*.” *The Anatomical Record* 297 (9): 1548–59. https://doi.org/10.1002/ar.22965.

Ono, Shoichiro, and David Pruyne. 2012. “Biochemical and Cell Biological Analysis of Actin in the Nematode Caenorhabditis Elegans.” *METHODS* 56 (1): 11–17.

Oosterheert, Wout, Florian E. C. Blanc, Ankit Roy, Alexander Belyy, Micaela Boiero Sanders, Oliver Hofnagel, Gerhard Hummer, Peter Bieling, and Stefan Raunser. 2023. “Molecular Mechanisms of Inorganic-Phosphate Release from the Core and Barbed End of Actin Filaments.” *Nature Structural & Molecular Biology* 30 (11): 1774–85. https://doi.org/10.1038/s41594-023-01101-9.

Pacquelet, Anne, Perrine Uhart, Jean-Pierre Tassan, and Grégoire Michaux. 2015. “PAR-4 and Anillin Regulate Myosin to Coordinate Spindle and Furrow Position during Asymmetric Division.” *Journal of Cell Biology* 210 (7): 1085–99. https://doi.org/10.1083/jcb.201503006.

Paix, A, A Folkmann, D Rasoloson, and G Seydoux. 2015. “High Efficiency, Homology-Directed Genome Editing in Caenorhabditis Elegans Using CRISPR-Cas9 Ribonucleoprotein Complexes.” *Genetics* 201 (1): 47–54.

Parker, Francine, Thomas G. Baboolal, and Michelle Peckham. 2020. “Actin Mutations and Their Role in Disease.” *International Journal of Molecular Sciences* 21 (9): 3371. https://doi.org/10.3390/ijms21093371.

Pasturel, Aurélien, Pierre-Olivier Strale, and Vincent Studer. 2020. “Tailoring Common Hydrogels into 3D Cell Culture Templates.” *Advanced Healthcare Materials* 9 (18): 2000519. https://doi.org/10.1002/adhm.202000519.

Patrinostro, Xiaobai, Pallabi Roy, Angus Lindsay, Christopher M. Chamberlain, Lauren J. Sundby, Colby G. Starker, Daniel F. Voytas, James M. Ervasti, and Benjamin J. Perrin. 2018. “Essential Nucleotide- and Protein-Dependent Functions of *Actb* /β-Actin.” *Proceedings of the National Academy of Sciences* 115 (31): 7973–78. https://doi.org/10.1073/pnas.1807895115.

Pettersen, Eric F., Thomas D. Goddard, Conrad C. Huang, Elaine C. Meng, Gregory S. Couch, Tristan I. Croll, John H. Morris, and Thomas E. Ferrin. 2021. “UCSF ChimeraX: Structure Visualization for Researchers, Educators, and Developers.” *Protein Science: A Publication of the Protein Society* 30 (1): 70–82. https://doi.org/10.1002/pro.3943.

Polubothu, S., D. Abdin, M. Barysch, A. Thomas, N. Bulstrode, R. Evans, L. Solman, et al. 2020. “Dermatological Signs Lead to Discovery of Mosaic ACTB Variants in Segmental Odontomaxillary Dysplasia.” *The British Journal of Dermatology* 183 (6): 1128–30. https://doi.org/10.1111/bjd.19339.

Priess, J. R., and D. I. Hirsh. 1986. “Caenorhabditis Elegans Morphogenesis: The Role of the Cytoskeleton in Elongation of the Embryo.” *Developmental Biology* 117 (1): 156–73. https://doi.org/10.1016/0012-1606(86)90358-1.

Procaccio, Vincent, Gloria Salazar, Shoichiro Ono, Melanie L. Styers, Marla Gearing, Antonio Davila, Richard Jimenez, et al. 2006. “A Mutation of Beta -Actin That Alters Depolymerization Dynamics Is Associated with Autosomal Dominant Developmental Malformations, Deafness, and Dystonia.” *American Journal of Human Genetics* 78 (6): 947–60. https://doi.org/10.1086/504271.

Quintin, Sophie, Shaohe Wang, Julien Pontabry, Ambre Bender, François Robin, Vincent Hyenne, Frédéric Landmann, Christelle Gally, Karen Oegema, and Michel Labouesse. 2018. “Correction: Non-Centrosomal Epidermal Microtubules Act in Parallel to LET-502/ROCK to Promote *C. Elegans* Elongation (Doi:10.1242/Dev.126615).” *Development* 145 (10): dev167262. https://doi.org/10.1242/dev.167262.

Reymann, Anne-Cecile, Fabio Staniscia, Anna Erzberger, Guillaume Salbreux, and Stephan W Grill. 2016. “Cortical Flow Aligns Actin Filaments to Form a Furrow.” *eLife* 5 (October):e17807.

Reynolds, Matthew J., Carla Hachicho, Ayala G. Carl, Rui Gong, and Gregory M. Alushin. 2022. “Bending Forces and Nucleotide State Jointly Regulate F-Actin Structure.” *Nature* 611 (7935): 380–86. https://doi.org/10.1038/s41586-022-05366-w.

Riva, Claudia, Martina Hajduskova, Christelle Gally, Shashi Kumar Suman, Arnaud Ahier, and Sophie Jarriault. 2022. “A Natural Transdifferentiation Event Involving Mitosis Is Empowered by Integrating Signaling Inputs with Conserved Plasticity Factors.” *Cell Reports* 40 (12): 111365. https://doi.org/10.1016/j.celrep.2022.111365.

Rivière, Jean-Baptiste, Bregje W M Van Bon, Alexander Hoischen, Stanislav S Kholmanskikh, Brian J O’Roak, Christian Gilissen, Sabine Gijsen, et al. 2012. “De Novo Mutations in the Actin Genes ACTB and ACTG1 Cause Baraitser-Winter Syndrome.” *Nature Genetics* 44 (4): 440–44. https://doi.org/10.1038/ng.1091.

Rose, Lesilee, and Pierre Gönczy. 2014. “Polarity Establishment, Asymmetric Division and Segregation of Fate Determinants in Early C. Elegans Embryos.” *WormBook*, 1–43.

Rubenstein, Peter A., and Kuo‐Kuang Wen. 2014. “Insights into the Effects of Disease‐causing Mutations in Human Actins.” *Cytoskeleton* 71 (4): 211–29. https://doi.org/10.1002/cm.21169.

Schafer, William. 2005. “Egg-Laying.” *WormBook*.

Schutt, Clarence E., James C. Myslik, Michael D. Rozycki, Nalin C. W. Goonesekere, and Uno Lindberg. 1993. “The Structure of Crystalline Profilin–β-Actin.” *Nature* 365 (6449): 810–16. https://doi.org/10.1038/365810a0.

Serobyan, Vahan, Zacharias Kontarakis, Mohamed A El-Brolosy, Jordan M Welker, Oleg Tolstenkov, Amr M Saadeldein, Nicholas Retzer, Alexander Gottschalk, Ann M Wehman, and Didier Yr Stainier. 2020. “Transcriptional Adaptation in Caenorhabditis Elegans.” *eLife* 9 (January):e50014. https://doi.org/10.7554/eLife.50014.

Skogseid, Inger Marie, Oddveig Røsby, Ane Konglund, James P. Connelly, Bård Nedregaard, Greg Eigner Jablonski, Nadja Kvernmo, Asbjørg Stray-Pedersen, and Joel C. Glover. 2018. “Dystonia-Deafness Syndrome Caused by ACTB p.Arg183Trp Heterozygosity

Shows Striatal Dopaminergic Dysfunction and Response to Pallidal Stimulation." *Journal of Neurodevelopmental Disorders* 10 (1): 17. https://doi.org/10.1186/s11689-018-9235-z.

Vanslembrouck, Bieke, Christophe Ampe, and Jolanda Van Hengel. 2020. "Time for Rethinking the Different B-actin Transgenic Mouse Models?" *Cytoskeleton* 77 (12): 527–43. https://doi.org/10.1002/cm.21647.

Vedula, Pavan, Satoshi Kurosaka, Nicolae Adrian Leu, Yuri I Wolf, Svetlana A Shabalina, Junling Wang, Stephanie Sterling, Dawei W Dong, and Anna Kashina. 2017. "Diverse Functions of Homologous Actin Isoforms Are Defined by Their Nucleotide, Rather than Their Amino Acid Sequence." *eLife* 6 (December):e31661. https://doi.org/10.7554/eLife.31661.

Verloes, Alain, Nataliya Di Donato, Julien Masliah-Planchon, Marjolijn Jongmans, Omar A. Abdul-Raman, Beate Albrecht, Judith Allanson, et al. 2015. "Baraitser–Winter Cerebrofrontofacial Syndrome: Delineation of the Spectrum in 42 Cases." *European Journal of Human Genetics* 23 (3): 292–301. https://doi.org/10.1038/ejhg.2014.95.

Verloes, Alain, Séverine Drunat, Daniela Pilz, and Nataliya Di Donato. 1993. "Baraitser-Winter Cerebrofrontofacial Syndrome." In *GeneReviews®*, edited by Margaret P. Adam, Jerry Feldman, Ghayda M. Mirzaa, Roberta A. Pagon, Stephanie E. Wallace, Lora JH Bean, Karen W. Gripp, and Anne Amemiya. Seattle (WA): University of Washington, Seattle. http://www.ncbi.nlm.nih.gov/books/NBK327153/.

Vontell, Regina, Veena G. Supramaniam, Alice Davidson, Claire Thornton, Andreas Marnerides, Muriel Holder-Espinasse, Suzanne Lillis, et al. 2019. "Post-Mortem Characterisation of a Case With an ACTG1 Variant, Agenesis of the Corpus Callosum and Neuronal Heterotopia." *Frontiers in Physiology* 10. https://www.frontiersin.org/journals/physiology/articles/10.3389/fphys.2019.00623.

Vuong-Brender, Thanh Thi Kim, Martine Ben Amar, Julien Pontabry, and Michel Labouesse. 2017. "The Interplay of Stiffness and Force Anisotropies Drives Embryo Elongation." *eLife* 6 (February):e23866. https://doi.org/10.7554/eLife.23866.

Vuong-Brender, Thanh T.K., Xinyi Yang, and Michel Labouesse. 2016. "C. Elegans Embryonic Morphogenesis." In *Current Topics in Developmental Biology*, 116:597–616. Elsevier. https://doi.org/10.1016/bs.ctdb.2015.11.012.

Waterhouse, Andrew, Martino Bertoni, Stefan Bienert, Gabriel Studer, Gerardo Tauriello, Rafal Gumienny, Florian T Heer, et al. 2018. "SWISS-MODEL: Homology Modelling of Protein Structures and Complexes." *Nucleic Acids Research* 46 (W1): W296–303. https://doi.org/10.1093/nar/gky427.

Wilkinson, Alex W., Jonathan Diep, Shaobo Dai, Shuo Liu, Yaw Shin Ooi, Dan Song, Tie-Mei Li, et al. 2019. "SETD3 Is an Actin Histidine Methyltransferase That Prevents Primary Dystocia." *Nature* 565 (7739): 372–76. https://doi.org/10.1038/s41586-018-0821-8.

Willis, John H., Edwin Munro, Rebecca Lyczak, and Bruce Bowerman. 2006. "Conditional Dominant Mutations in the Caenorhabditis Elegans Gene Act-2 Identify Cytoplasmic and Muscle Roles for a Redundant Actin Isoform." *Molecular Biology of the Cell* 17 (3): 1051–64. https://doi.org/10.1091/mbc.e05-09-0886.

Yemini, Eviatar, Albert Lin, Amin Nejatbakhsh, Erdem Varol, Ruoxi Sun, Gonzalo E. Mena, Aravinthan D.T. Samuel, Liam Paninski, Vivek Venkatachalam, and Oliver Hobert. 2021. "NeuroPAL: A Multicolor Atlas for Whole-Brain Neuronal Identification in C. Elegans." *Cell* 184 (1): 272-288.e11. https://doi.org/10.1016/j.cell.2020.12.012.

Zech, Michael, Robert Jech, Matias Wagner, Tobias Mantel, Sylvia Boesch, Michael Nocker, Angela Jochim, et al. 2017. "Molecular Diversity of Combined and Complex Dystonia: Insights from Diagnostic Exome Sequencing." *Neurogenetics* 18 (4): 195–205. https://doi.org/10.1007/s10048-017-0521-9.

Zhang, Pu, Taylor N. Medwig-Kinney, and Bob Goldstein. 2023. “Architecture of the Cortical Actomyosin Network Driving Apical Constriction in *C. Elegans*.” *Journal of Cell Biology* 222 (9): e202302102. https://doi.org/10.1083/jcb.202302102.

Figure legends

Figure 1 : Insertion of Non-Muscle Actinopathies variants in the *C. elegans act-2*

A : Structural model of ACT-2 G-actin generated by Alphafold2. Subdomains of ACT-2 are colored in grey (SD1), light grey (SD2), blue (SD3) and light blue (SD4). Homology model of the ACT-2 filament (based on PDB-ID: 8DNH). ACT-2 protomers are colored in different shades of blue. The mutated residues investigated in this study are shown in red. The ATP bound to the individual protomers is shown as a stick-model. The zoom-in shows the location and structural environment of the individual mutated residues in more detail.

B : Schematic *act-2* representation highlighting the loci of single point variants obtained via CRISPR edition (Adapted from http://wormweb.org/exonintron). Three *act-2* gene knockouts are also depicted : *rey016*, *rey021* and *ok1229* (Willis et al., 2006). Note that the amino acid numbering is here in frame with human ACTB/ACTG1, consider -1 AA in the frame of *C. elegans* due to an additional cysteine in second N-ter position, the base pair are however kept in the *C. elegans act-2* frame.

C : Dot heatmap of patients' symptoms. Intellectual disability (ID) level letter code : n=none, m=mild, mo=moderate, s=severe, p=profound. MRI = Magnetic Resonance Imaging. BWCFF = Baraitser-Winter Cerebro Fronto Facial syndrome.

D : Table summarizing the overall viability of *C. elegans act-2* variants at 20°C.

Figure S1 :

A : Amino acid alignment of *C. elegans'* ACT-2, human ACTB and ACTG1 showing high conservation of amino acid as well as amino acid physico-chemical properties (Snapgene). Loci of interest are framed with black boxes.

B : Alignment of sequences obtained from the sequencing of F1 animals from the CRISPR/Cas9 *act-2* p.G74V generation show the presence of the Gly to Ser variant (Snapgene, black box). Top rows show the reference *act-2* sequence and its translation. Bottom rows show the obtained sequence, peaks and predicted translation.

Figure 2 : *act-2* gene knock-outs affects fertility despite compensation mechanisms

A : Single animal RT-qPCR showing the normalized amount of mRNA for each *C. elegans* actin coding genes in the *act-2* homozygous *ok1229* and *rey021*. Normalization was done with the amount of mRNA quantified for the housekeeping gene *iscu-1* and with the WT values set to 1. Different colors show different replicates. Small dot is the value for one animal while bigger dots correspond to the experiment's mean. Diamonds show the mean of all replicates.

B : Progeny number of homozygous *act-2* KO (*ok1229* and *rey021*) at the mentioned temperatures were counted during 48h. The sum of eggs laid for one animal is shown as a dot

or a triangle. B' : Percentage of eggs that failed to hatch. The mean number of eggs that did not hatch for one animal is shown as a dot or a triangle. Mean value is represented by a diamond.

C : Progeny number at 20°C were counted for 72h for homozygous (*rey016*/*rey016*) (*rey021*/*rey021*) or heterozygous (*rey016*/+) (*rey021*/+) *act-2* KO animals. The sum of eggs laid for one animal is shown as a dot. C' : Percentage of eggs that failed to hatch. The mean number of eggs that did not hatch for one animal is shown as a dot. Mean value is represented by a diamond.

Figure S2 :

A : Standard curve analysis to determine the efficiency of amplification of the 6 primer pairs used for RT-qPCR. Efficiency is calculated using $E = 10^{\frac{1}{slope}}$.

Figure 3 : *act-2* variants affect egg-laying capacities and embryogenesis success

A : Progeny number at 20°C were counted for 72h for homozygous *act-2* variants. The sum of eggs laid for one animal is shown as a dot. Mean is represented as a diamond.

B : Percentage of eggs that failed to hatch. The percent of dead eggs for one animal is shown as a dot. Mean is represented as a diamond. The rightmost plot presents the 95% credibility intervals of the posterior distributions of the embryonic lethality rates considering the priors described in the methods section and our observed data set. These are calculated with a Bayesian model based on Poisson laws with an offset to take into account the progeny numbers. Experimental values are represented by red diamonds (mean) and blue circles (median).

C : Actin organization in a WT gonad observed using an actin probe (LifeAct::mKate2). Green and purple arrows represent the space measured to calculate the rachis/gonad ratio measured in front of the -1 oocyte.

D : Boxplot presenting the ratio between the rachis and the gonad's width of homozygote animals. Mean is represented as a diamond.

E : Heatmap of observed phenotypes, in percent.

F : Stacked histogram of the end status of embryogenesis for different *act-2* variants in percent. Schemes on the right represent the different defects observed. * embryos coming from heterozygous balanced animals. (See Movies 1, 2, 3, 4 and 5).

Figure S3 :

A : Progeny number at 20°C were counted for 72h for heterozygous *act-2* variant animals. The sum of eggs laid for one animal is shown as a dot. Mean is represented as a diamond.

B : Percentage of eggs that failed to hatch. The mean number of eggs that did not hatch for one animal is shown as a dot. Mean is represented as a diamond.

C & D : Red boxes show the area where no WT eggshells are present. Red points show embryos that will subsequently die while blue triangles mean that the embryo will survive. Embryo schemes above are at the right scale. * embryos coming from heterozygous balanced animals. C: Aspect ratio measurement of embryos' eggshell. Aspect ratio is defined as the ratio between the major and minor axis. D: 2D Area measurement of embryos' eggshell.

E : Timeline of recognizable morphogenesis stages during *C. elegans'* embryogenesis. Time counted after fertilization, from (Hall, D.H., Herndon, L.A., and Altun, Z. 2017).

Leftmost plot presents the timing in minutes between the bean stage and the comma stage. Rightmost plot presents the timing in minutes between the comma stage and hatching. * embryos coming from heterozygous balanced animals.

Figure 4 : Actin mutation effects on cortical organization in early embryos

A : Cortical plane of embryos at different stages, LifeAct::mKate2 shown in magenta and NMY-2::GFP shown in green, to reveal actin filaments and myosin distribution. p.T203M animals only have LifeAct::mKate2. (PN = Pronuclei) Anterior is on the left.

B, C, D : Equatorial plane image of embryos expressing LifeAct::mKate2 (magenta) and NMY-2::GFP (green)

B : Cytokinesis defect observed. The cytokinesis ring relaxes after completion of a first ingression (pink arrow), cytokinesis then proceeds to divide directly the zygote in four cells. See Movie 6.

C : Meiosis defects. An additional nucleus is visible (blue arrow). Nuclei are circled. See Movie 7.

D : Blebbing. Large protrusion called bleb extrude from the anterior cell (orange arrow). After actin and myosin reassembly the bleb retracts and division seems to occur normally. See Movie 8.

E : Abnormal membrane ruffling is observed in some embryos (white arrow).

F : Cortical plane of embryos presenting other phenotypes. Abnormal aspect ratio of the cortex implies a rounder embryo (see also Figure S4). Abnormal division axis (red arrows) leads to abnormal cell-cell contacts. Breaks in cortex are highlighted by green arrows.

Scale bar is 10µm.

Figure S4 :

Size of the anterior cell AB (Magenta arrow) divided by the embryo's size (Green arrow) in percent.

Figure 5 : Actin mutations can affect muscle function and/or neuronal cell number

A : 3D animal migration assay. Percentage of animals reaching a chemoattractant after migration inside a pluronic gel, monitored every 15 minutes for 2 hours. Results for individual wells (N) for each variant are visible as transparent dots, n is the total number of animals assessed and bars show the standard deviation. The final proportion for each variant was compared to that of WT in the frame of Bayesian statistics, using two binomial distributions. The odds ratio (OR) as well as the probability (p) that the difference is superior to 0.2 are indicated.

B : Variation of the neuronal cell number are observed in *act-2* variant conditions. Reconstructed image of an animal expressing the NeuroPal transgene. Insets show representative images of identified defects compared to the WT *act-2* reference: presence of a micronucleus (Orange), an extra (Magenta) or a missing cell (Green). Scale bar is 50 µm.

C : Summary of neuronal phenotypes observed in the actin variants.

Figure S5 :

Chemotaxis assay. The chemotaxis index is calculated $I = \frac{n_{OP50} - n_{H_2O}}{n_{Total} - n_{immobile\ animals}}$ and show the proportion of animals chemoattracted to concentrated OP50 (100mg/mL) (in red). Blue bars show the percentage of animals that did not move from where they were placed for the assay.

Figure 6 : Data integration to build a comparative tool

Principal Component Analysis plot of analysed actin variant animals reveal clusters which can be associated to classes of phenotypes. Corresponding table with data is available in Figure S6A. p.G74V was added manually as no data could be retrieved for this strain. Arrows link homozygotes to their respective heterozygotes.

Figure S6 :

A : Variables used for to build the Principal Component Analysis plot presented in Figure 6, as well as their quality of representation in each dimension (cos2).

B : Principal Component Analysis plot of analysed actin variant animals using variables quantified without introducing fluorescent reporters. p.G74V was added manually as no data can be retrieved for this strain. Arrows link homozygotes to their respective heterozygotes.

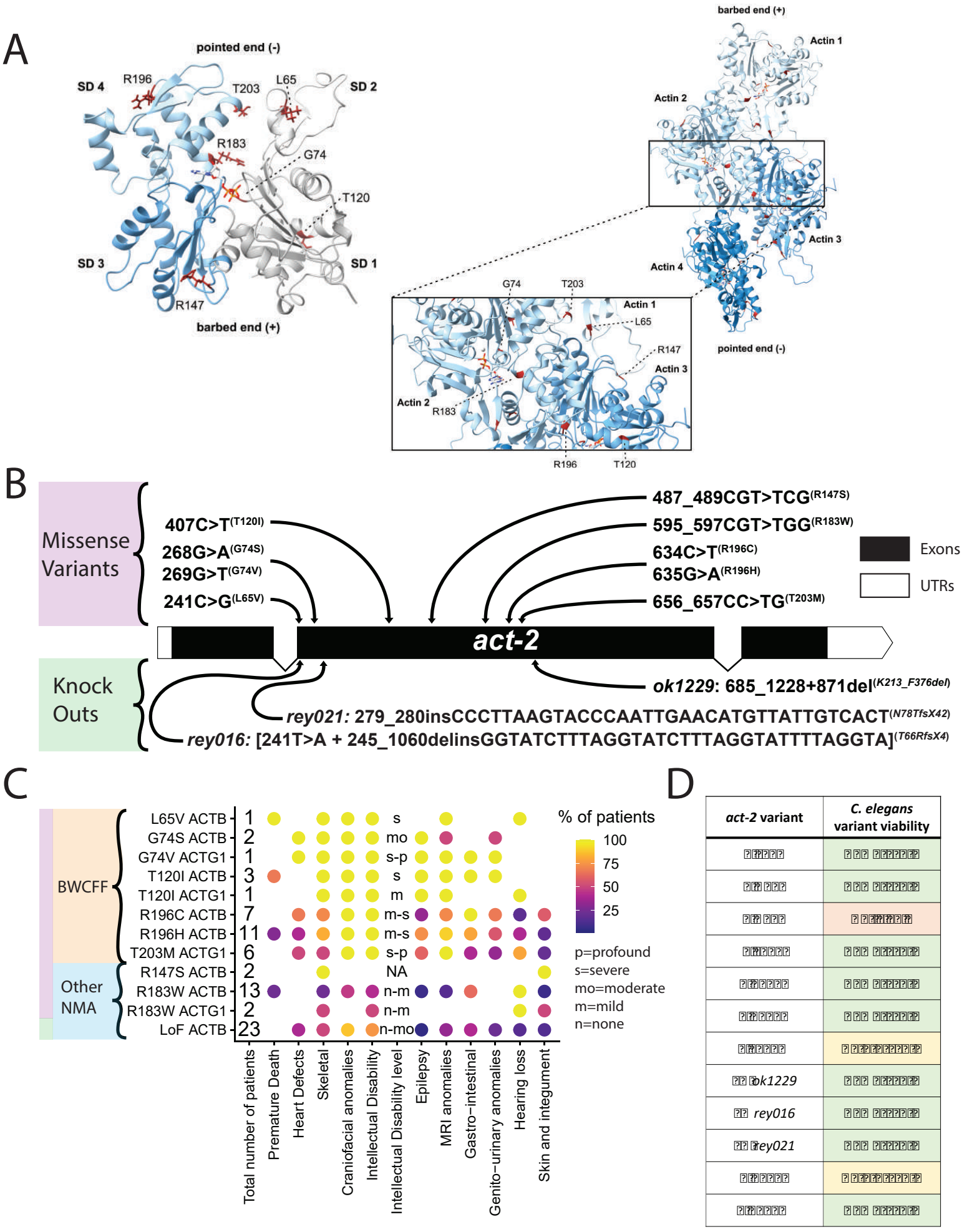
A
pointed end (-)
SD 4
R196
T203
L65
SD 2
R183
G74
T120
SD 3
SD 1
R147
barbed end (+)
barbed end (+)
Actin 1
Actin 2
Actin 3
Actin 4
pointed end (-)
G74
T203
Actin 1
L65
R147
Actin 3
Actin 2
R183
R196
T120
B
Missense Variants
407C>T(T120I)
268G>A(G74S)
269G>T(G74V)
241C>G(L65V)
487_489CGT>TCG(R147S)
595_597CGT>TGG(R183W)
634C>T(R196C)
635G>A(R196H)
656_657CC>TG(T203M)
Exons
UTRs
act-2
Knock Outs
ok1229: 685_1228+871del(K213_F376del)
rey021: 279_280insCCCTTAAGTACCCAATTGAACATGTTATTGTCACT(N78TfsX42)
rey016: [241T>A + 245_1060delinsGGTATCTTTAGGTATCTTTAGGTATTTTAGGTA](T66RfsX4)
C
BWCFF
Other NMA
L65V ACTB 1 s
G74S ACTB 2 mo
G74V ACTG1 1 s-p
T120I ACTB 3 s
T120I ACTG1 1 m
R196C ACTB 7 m-s
R196H ACTB 11 m-s
T203M ACTG1 6 s-p
R147S ACTB 2 NA
R183W ACTB 13 n-m
R183W ACTG1 2 n-m
LoF ACTB 23 n-mo
Total number of patients
Premature Death
Heart Defects
Skeletal
Craniofacial anomalies
Intellectual Disability
Intellectual Disability level
Epilepsy
MRI anomalies
Gastro−intestinal
Genito−urinary anomalies
Hearing loss
Skin and integument
% of patients
100
75
50
25
p=profound
s=severe
mo=moderate
m=mild
n=none
D
act-2 variant
C. elegans variant viability
ok1229
rey016
rey021

Figure 1

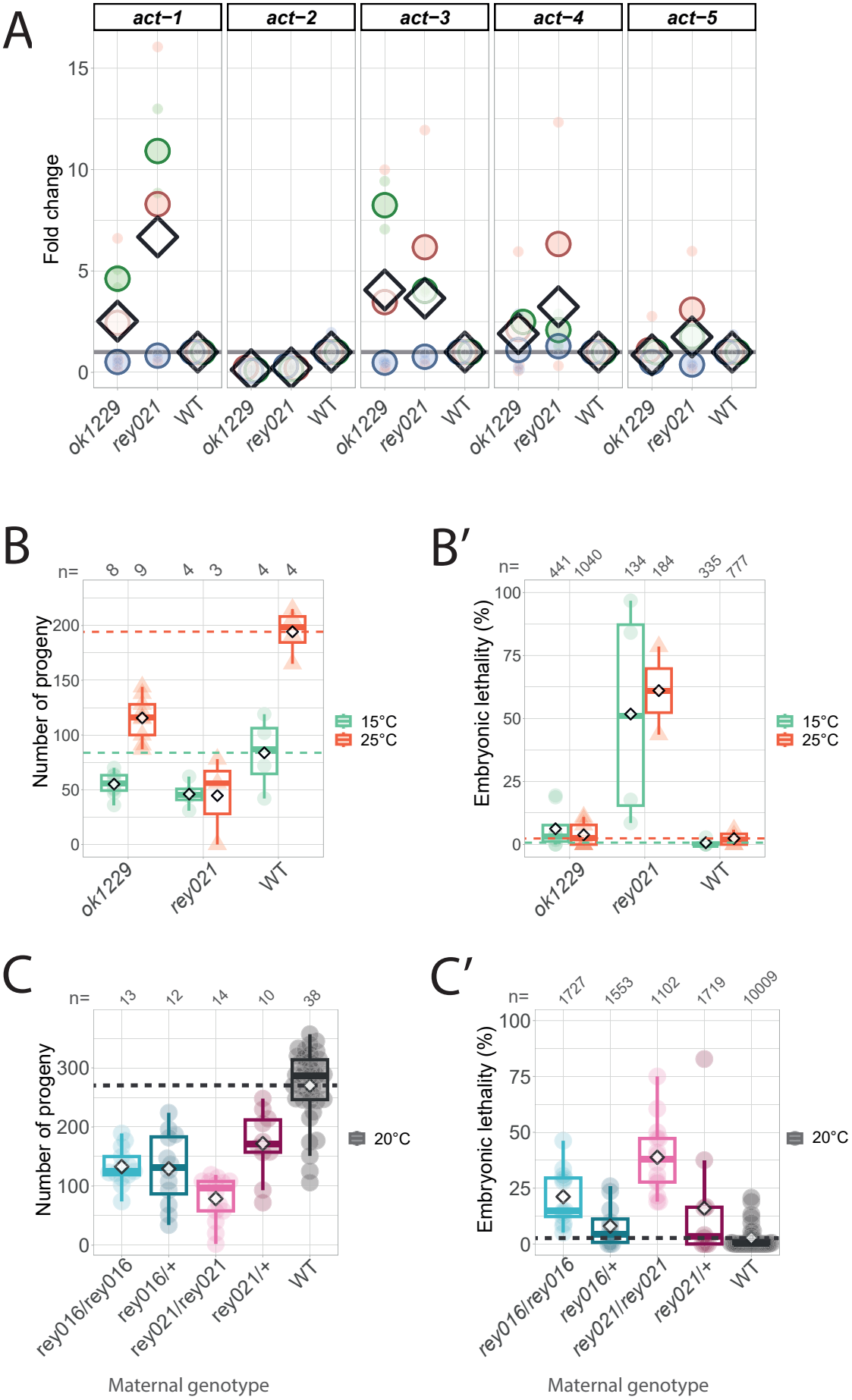
A
act−1
act−2
act−3
act−4
act−5
Fold change
15
10
5
0
ok1229
rey021
WT
B
n=
8
9
4
3
4
4
Number of progeny
200
150
100
50
0
15°C
25°C
B′
n=
441
1040
134
184
335
777
Embryonic lethality (%)
100
75
50
25
0
C
n=
13
12
14
10
38
300
20°C
rey016/rey016
rey016/+
rey021/rey021
rey021/+
Maternal genotype
C′
1727
1553
1102
1719
10009

Figure 2

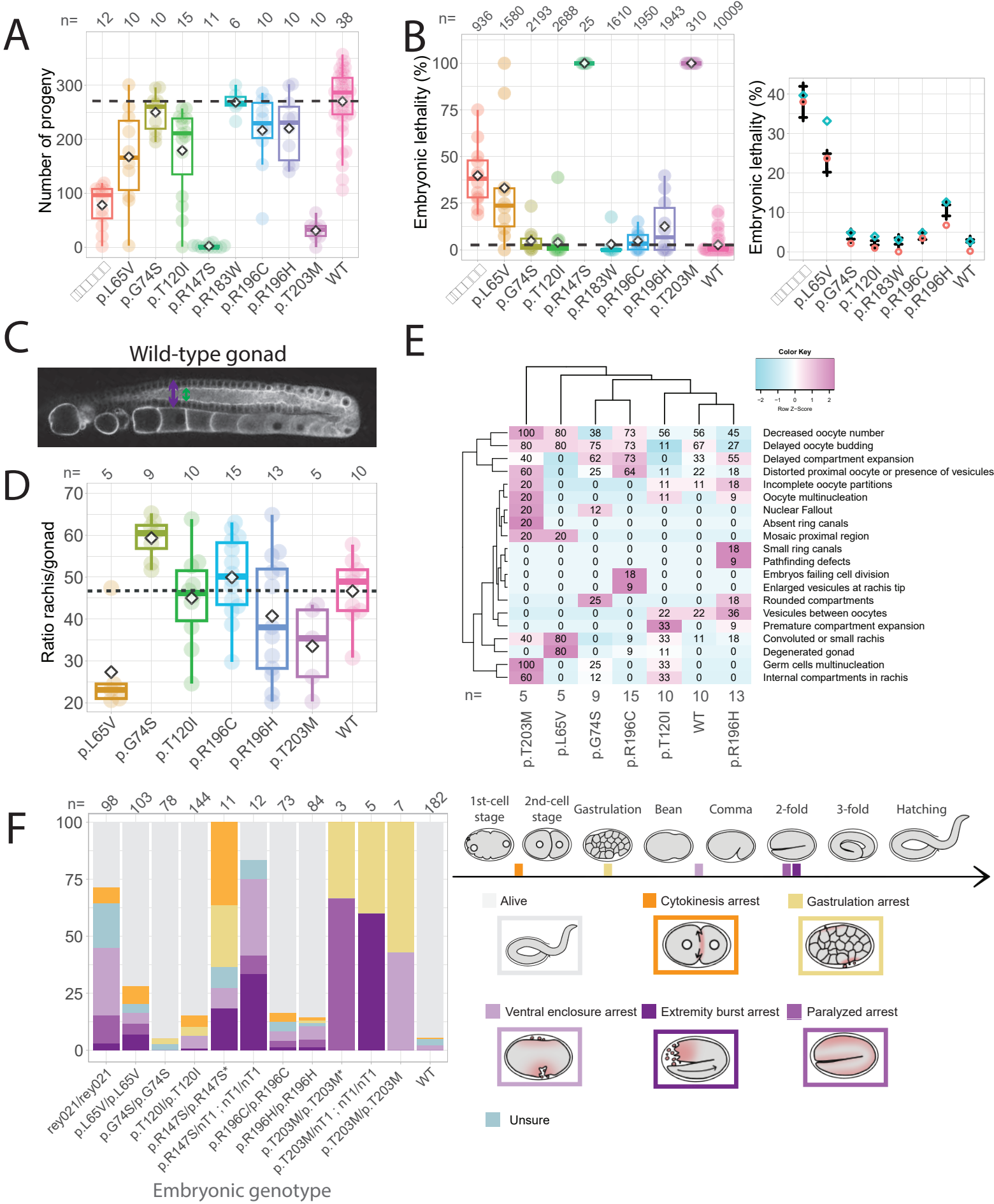
A
n= 12 10 10 15 11 6 10 10 10 38
Number of progeny
0 100 200 300
p.L65V p.G74S p.T120I p.R147S p.R183W p.R196C p.R196H p.T203M WT
B
n= 936 1580 2193 2688 25 1610 1950 1943 310 10009
Embryonic lethality (%)
0 25 50 75 100
p.L65V p.G74S p.T120I p.R147S p.R183W p.R196C p.R196H p.T203M WT
Embryonic lethality (%)
0 10 20 30 40
p.L65V p.G74S p.T120I p.R183W p.R196C p.R196H WT
C
Wild-type gonad
D
n= 5 9 10 15 13 5 10
Ratio rachis/gonad
20 30 40 50 60 70
p.L65V p.G74S p.T120I p.R196C p.R196H p.T203M WT
E
Color Key
Row Z-Score
Decreased oocyte number 100 80 38 73 56 56 45
Delayed oocyte budding 80 80 75 73 11 67 27
Delayed compartment expansion 40 0 62 73 0 33 55
Distorted proximal oocyte or presence of vesicules 60 0 25 64 11 22 18
Incomplete oocyte partitions 20 0 0 0 11 11 18
Oocyte multinucleation 20 0 0 0 11 0 9
Nuclear Fallout 20 0 12 0 0 0 0
Absent ring canals 20 0 0 0 0 0 0
Mosaic proximal region 20 20 0 0 0 0 0
Small ring canals 0 0 0 0 0 0 18
Pathfinding defects 0 0 0 0 0 0 9
Embryos failing cell division 0 0 0 18 0 0 0
Enlarged vesicules at rachis tip 0 0 0 9 0 0 0
Rounded compartments 0 0 25 0 0 0 18
Vesicules between oocytes 0 0 0 0 22 22 36
Premature compartment expansion 0 0 0 0 33 0 9
Convoluted or small rachis 40 80 0 9 33 11 18
Degenerated gonad 0 80 0 9 11 0 0
Germ cells multinucleation 100 0 25 0 33 0 0
Internal compartments in rachis 60 0 12 0 33 0 0
n= 5 5 9 15 10 10 13
p.T203M p.L65V p.G74S p.R196C p.T120I WT p.R196H
F
n= 98 103 78 144 11 12 73 84 3 5 7 182
100 75 50 25 0
rey021/rey021 p.L65V/p.L65V p.G74S/p.G74S p.T120I/p.T120I p.R147S/p.R147S* p.R147S/nT1 : nT1/nT1 p.R196C/p.R196C p.R196H/p.R196H p.T203M/p.T203M* p.T203M/nT1 : nT1/nT1 p.T203M/p.T203M WT
Embryonic genotype
1st-cell stage
2nd-cell stage
Gastrulation
Bean
Comma
2-fold
3-fold
Hatching
Alive
Cytokinesis arrest
Gastrulation arrest
Ventral enclosure arrest
Extremity burst arrest
Paralyzed arrest
Unsure

Figure 3

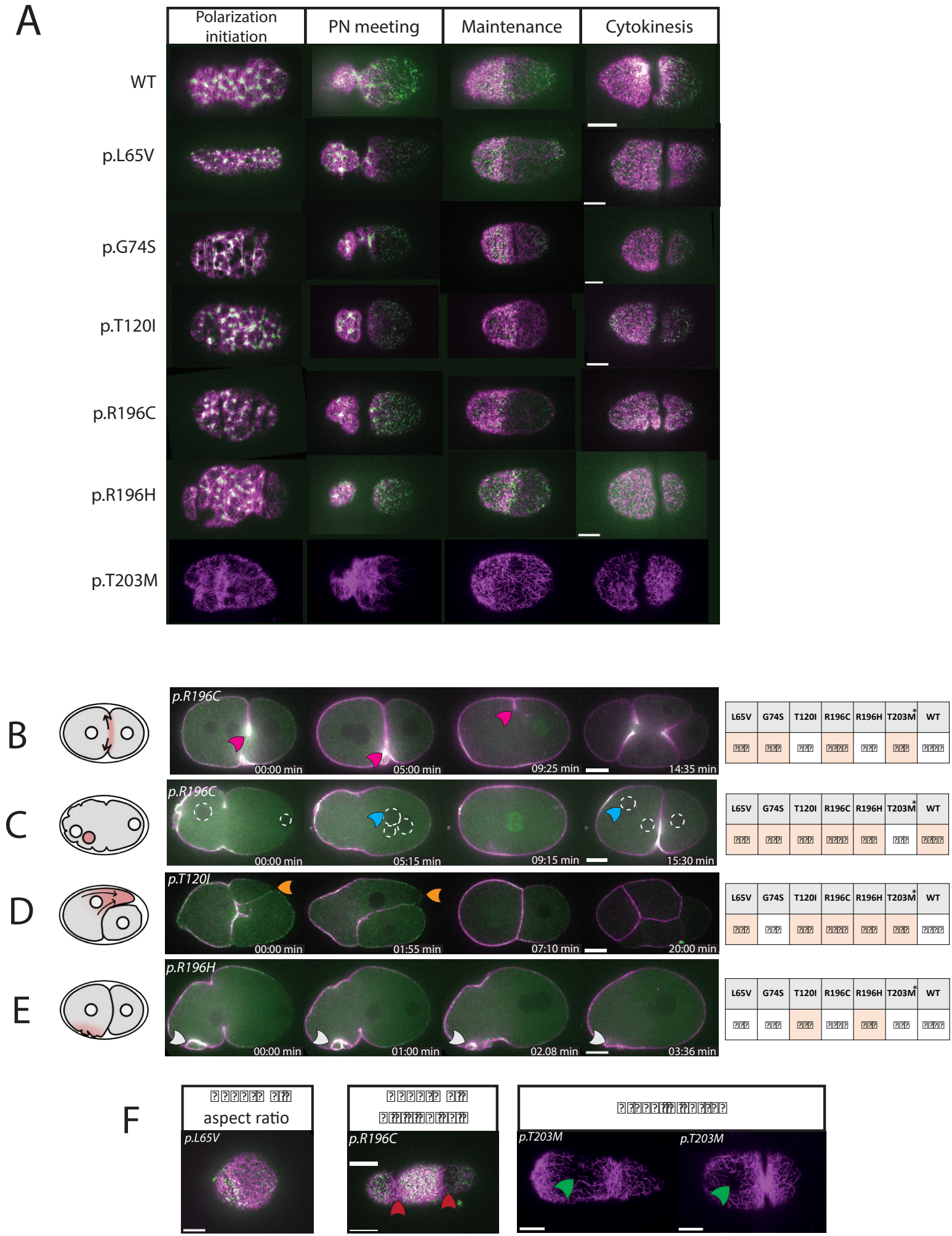
A
Polarization initiation
PN meeting
Maintenance
Cytokinesis
WT
p.L65V
p.G74S
p.T120I
p.R196C
p.R196H
p.T203M
B
p.R196C
00:00 min
05:00 min
09:25 min
14:35 min
C
p.R196C
00:00 min
05:15 min
09:15 min
15:30 min
D
p.T120I
00:00 min
01:55 min
07:10 min
20:00 min
E
p.R196H
00:00 min
01:00 min
02.08 min
03:36 min
L65V G74S T120I R196C R196H T203M* WT
F
aspect ratio
p.L65V
p.R196C
p.T203M
p.T203M

Figure 4

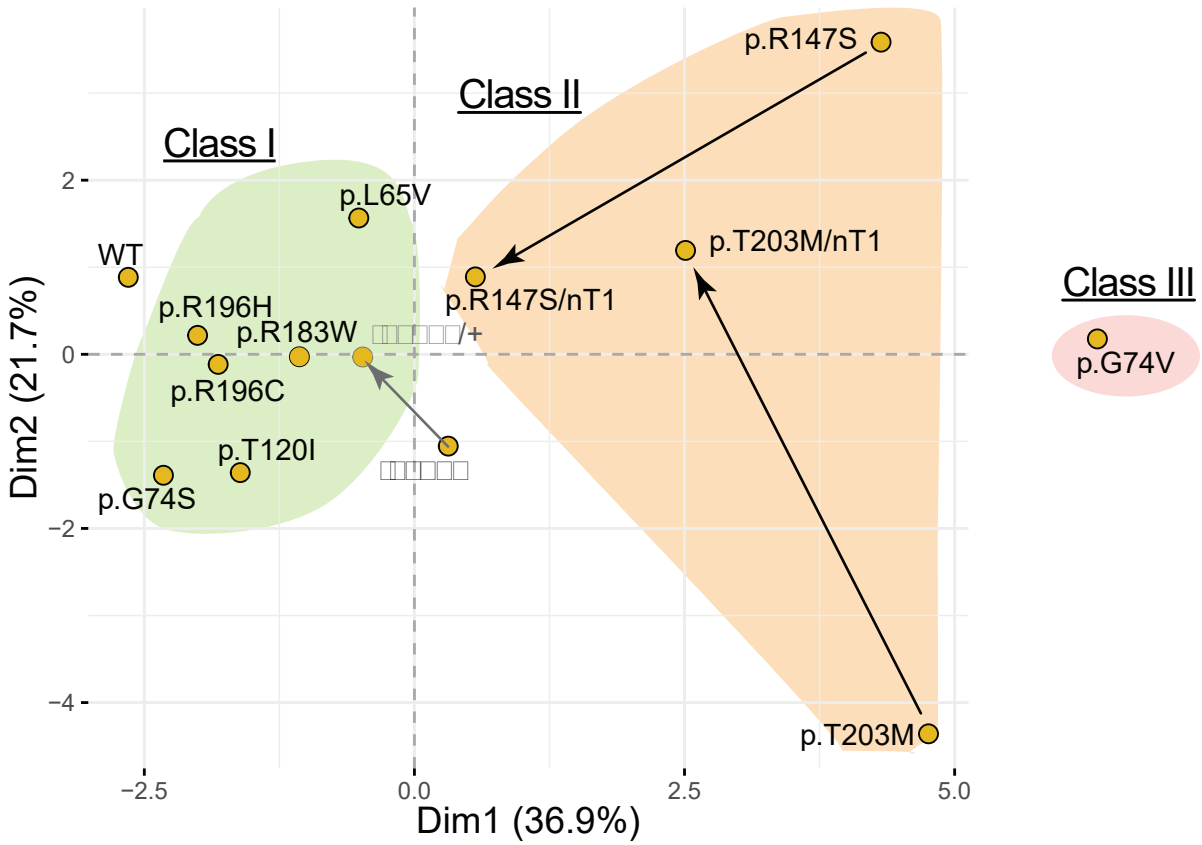
Class I
Class II
Class III
p.R147S
p.L65V
WT
p.T203M/nT1
p.R147S/nT1
p.R196H
p.R183W
/+
p.R196C
p.T120I
p.G74S
p.T203M
p.G74V
2
0
−2
−4
−2.5
0.0
2.5
5.0
Dim2 (21.7%)
Dim1 (36.9%)

Figure 6

A

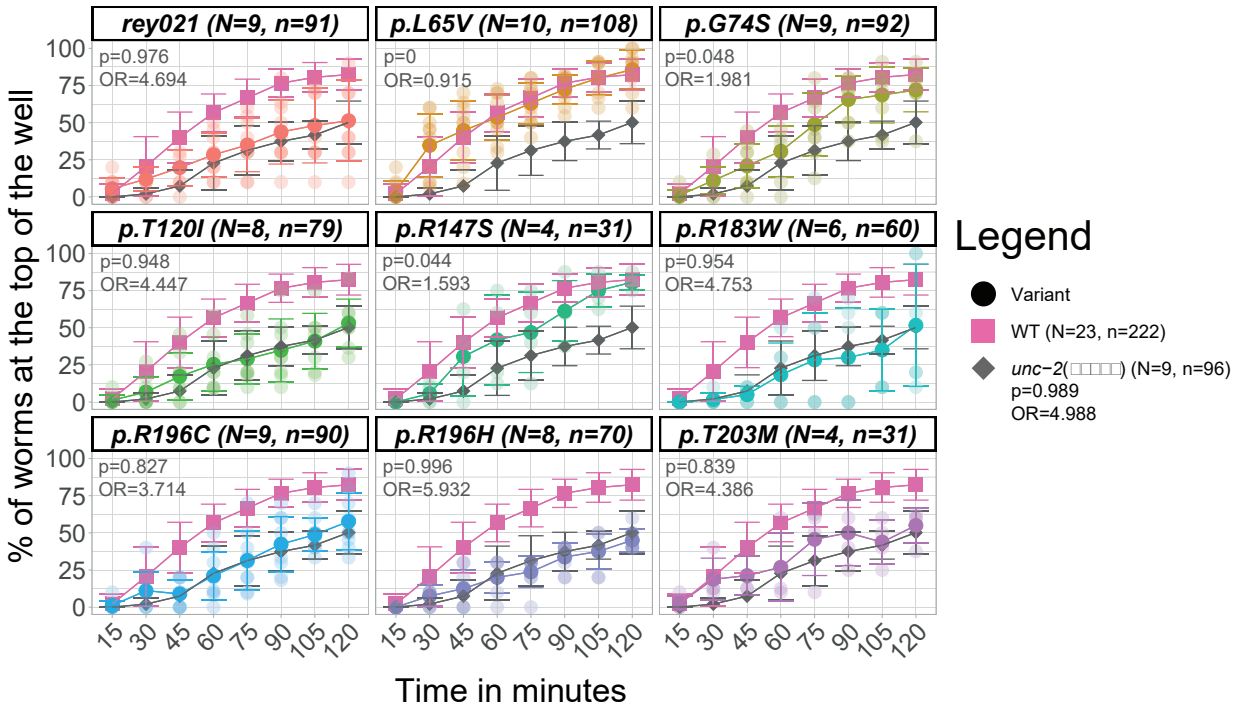

B

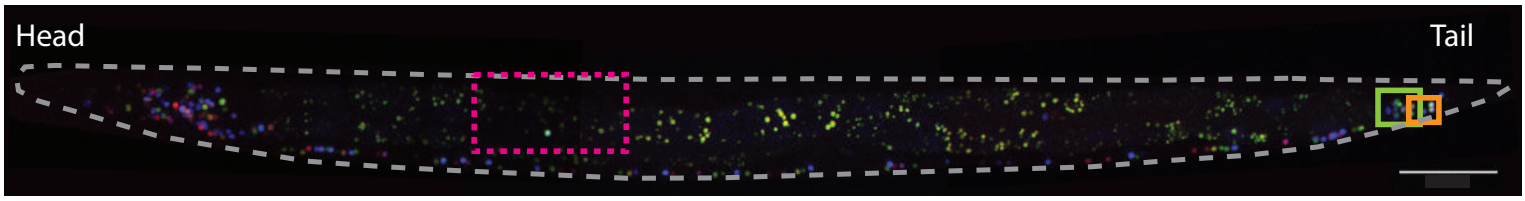

p.T120I

Additional neuronal cell (1/7)

p.R196C

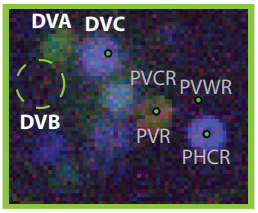

No DVB (1/15)

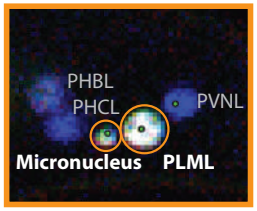

PLML micronucleus (1/15)

C

		L65V	G74S	T120I	R147S	R196C	R196H	T203M	*rey021*	WT
Additional Neuron	SDQR	0/8	0/7	1/7	0/8	1/6	0/3	0/2	1/6	0/5
	Other	1/14	1/14	0/16	0/14	0/15	0/15	1/4	1/15	0/14
Micronucleus		0/14	0/14	0/16	1/14	1/15	0/15	0/4	2/15	0/14
Missing Neuron	DVB	0/14	1/14	0/16	0/14	1/15	0/15	0/4	1/15	0/14
	PDA	0/14	1/14	0/16	0/14	0/15	0/15	0/4	0/15	0/14
	Other	0/14	1/14	3/16	1/14	0/15	0/15	1/4	2/15	0/14

Figure 5